# The Design Space of Plane Elastic Curves

CHRISTIAN HAFNER and BERND BICKEL, IST Austria

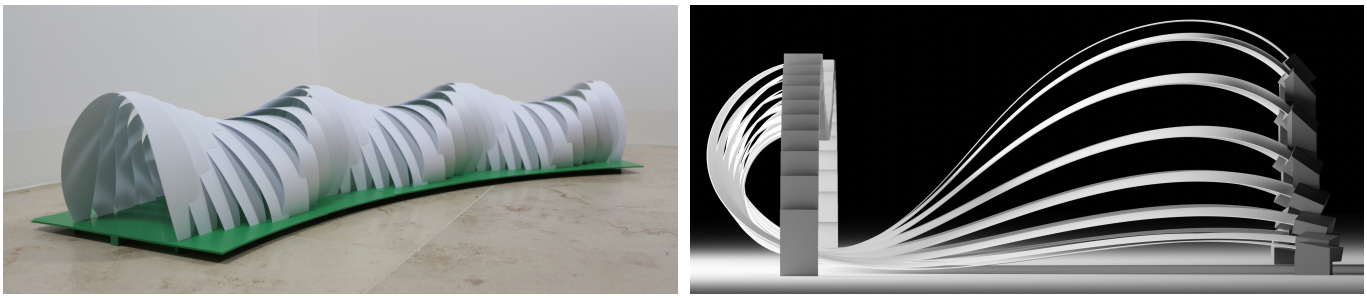

Fig. 1. **Pavilion and Carpet**. *Left*: Photograph of a physical pavilion model, constructed by bending inexpensive strips of plane cardboard. The flat outline of all strips is determined computationally within 0.3 seconds, in order to exactly match the design under their own weight. *Right*: Rendering of active-bending design for a free-form structure. The beam stiffness profiles adapt to design edits in real time, and a form-finding algorithm improves manufacturability.

Elastic bending of initially flat slender elements allows the realization and economic fabrication of intriguing curved shapes. In this work, we derive an intuitive but rigorous geometric characterization of the design space of plane elastic rods with variable stiffness. It enables designers to determine which shapes are physically viable with active bending by visual inspection alone. Building on these insights, we propose a method for efficiently designing the geometry of a flat elastic rod that realizes a target equilibrium curve, which only requires solving a linear program.

We implement this method in an interactive computational design tool that gives feedback about the feasibility of a design, and computes the geometry of the structural elements necessary to realize it within an instant. The tool also offers an iterative optimization routine that improves the fabricability of a model while modifying it as little as possible. In addition, we use our geometric characterization to derive an algorithm for analyzing and recovering the stability of elastic curves that would otherwise snap out of their unstable equilibrium shapes by buckling. We show the efficacy of our approach by designing and manufacturing several physical models that are assembled from flat elements.

CCS Concepts: • **Computing methodologies** → **Shape modeling**; **Modeling and simulation**; • **Theory of computation** → **Computational geometry**; • **Mathematics of computing** → *Mathematical optimization.*

Additional Key Words and Phrases: Elastic Rods, Computational Fabrication, Computational Design, Interactive Design, Active Bending

**ACM Reference Format:**
Christian Hafner and Bernd Bickel. 2021. The Design Space of Plane Elastic Curves. *ACM Trans. Graph.* 40, 4, Article 126 (August 2021), 20 pages. https://doi.org/10.1145/3450626.3459800

Authors' address: Christian Hafner, chafner@ist.ac.at; Bernd Bickel, bernd.bickel@ist.ac.at, IST Austria, Klosterneuburg, Am Campus 1, Austria, 3400.

Permission to make digital or hard copies of part or all of this work for personal or classroom use is granted without fee provided that copies are not made or distributed for profit or commercial advantage and that copies bear this notice and the full citation on the first page. Copyrights for third-party components of this work must be honored. For all other uses, contact the owner/author(s).
© 2021 Copyright held by the owner/author(s).
0730-0301/2021/8-ART126
https://doi.org/10.1145/3450626.3459800

## 1 INTRODUCTION

Slender beams in active bending allow the realization of intriguing structures, with innovative uses in the construction of frames and facades, furniture and product design, and even machine engineering, as seen in Fig. 2. Despite a firm grounding in history, such as its centuries-old role in the construction of Turkmen tents, the aesthetic of curves that emerge from pure bending still fascinates designers, architects, and mathematicians today [Lienhard et al. 2013].

The primary allure of bending as part of the formation process is its economic advantage: Curved members can be cut from flat, inexpensive sheets of elastic material such as plywood, which allows for easy transportation, and assembly on-site. This has the promise of reducing the need for an individual mold per unique structural member. Active bending also brings with it a singular design and form-finding challenge: The design space of shapes that can be physically realized is dictated by the underlying mechanics of slender beams. Insights about the geometric structure of this design space are therefore of practical value, because they can guide the intuition of the designer towards feasible designs. As we will show, they also open the door to extremely efficient optimization algorithms that further support the form-finding process.

The design space of slender beams in plane bending is related to the *Elastica problem*, a classical question in mechanics: Given a straight, slender structural element with constant stiffness, enumerate all its static equilibria in the plane. Originally posed by Bernoulli, a full enumeration as a one-parameter family was given by Saalschütz in terms of elliptic functions in 1880. This result has historically influenced the use of mechanical splines in design, but the assumption of constant stiffness limits the space of equilibrium curves attained within the Elastica framework.

Digital fabrication methods simplify the manufacture of structural elements with spatially varying cross-sectional profiles, and thus variable stiffness. Yet, we are unaware of any work that enumerates or classifies all shapes that can be attained as equilibrium states of variable-stiffness elastic curves. This suggests two questions: Is it possible to characterize all plane curves that can be attained as

Fig. 2. **Examples of Active Bending**. *Left to right, top to bottom:* ICD/ITKE Research Pavilion 2010 [Fleischmann and Menges 2011]. TR11 lamp by Tom Rossau. PS1 Loop, Boston, by Höweler + Yoon Architecture. Bentwood type "yourte" (CC BY 2.0 Jean-Pierre Dalbéra). Morphing rotor blade controlled by a servomotor (CC BY 3.0 DLR). Arc lamp [Cuvilliers et al. 2018].

static equilibria of slender beams? And how can we construct the geometry of a beam that realizes a given equilibrium curve?

In this work, we give positive answers to both questions. This results in a geometric characterization of all variable-stiffness elastic plane curves that is both intuitive and mathematically sharp. We also show a method to compute the stiffness profile required to realize a given elastic curve, which is globally optimal with respect to a convenient fabricability objective. These computations only take a fraction of a second, which makes them ideal for interactive design, where they provide immediate feedback about the practicality of a structure. At the same time, they can be integrated in iterative form-finding algorithms that suggest design trade-offs to the user at interactive speeds. We explore both use cases in this work.

For many real-world applications, the dead load and stability of a member play an important role in the design process. This is because a beam may deform considerably under its own weight, and an unstable element will even change its shape completely by snapping into a different equilibrium. These effects are not part of the classical Elastica model, but we show that the dead load can be incorporated into our construction method with virtually no penalty to computation time. The stability problem is more difficult and, in our experience, beyond the grasp of human intuition alone: It is often impossible to tell by visual inspection whether a given curve is stable, or even whether there could be a similar curve that is stable. We show that our geometric characterization of elastic curves is the key ingredient in designing an algorithm that can modify an unstable curve to yield a similar—and sometimes visually indistinguishable—stable curve.

Our contributions impact design with active bending in three profound ways. First, the geometric characterization of elastic curves informs a designer about the kinds of shapes that are physically possible within active-bending structures. This prevents infeasible designs even in the first phase of conception. Second, our gravity-aware construction method for stiffness profiles gives instant feedback about the practicality of a design. Namely, it tells us whether it can be realized with a given material and fabrication method. Third, we enable optimization routines that automatically improve the fabricability of a design with small changes to form—a process that takes under one second per beam in all of our examples.

## 2 RELATED WORK

Research in computer graphics has made extensive contributions to fabrication-aware design. They are covered by a number of comprehensive survey articles [Attene et al. 2018; Bermano et al. 2017; Bickel et al. 2018]. In the following, we will focus on work closely related to the simulation and design of rods and structures shaped from flat configurations.

### 2.1 Fabrication-Aware Design

*Geometry-based* methods explore the design of objects without explicitly considering forces in the system. Numerous design techniques have been developed for approximating shapes from flat sheets, for example based on folding [Dudte et al. 2016], curved developable surfaces [Ion et al. 2020; Stein et al. 2018], auxetic shells [Konaković-Luković et al. 2018], wire meshes mapped to the model of Chebyshev nets [Garg et al. 2014], or packable spirals that can be pulled apart [Wolff et al. 2018]. Pillwein et al. [2020] show that geodesic grids, spatial grids of bent lamellae, can be designed purely based on a set of problem-specific geometric conditions. For 4D printing, Wang et al. [2019] build on geometric abstractions of the actuation process of composite thermoplastics, and present an interactive system to directly specify composites and preview their actuation behavior.

Recently, Liu et al. [2020] proposed a method for designing elastic planar sheets that can be bent into axisymmetric 3d structures without gaps. Their approach relies on elastic strips whose thickness and width are tapered. This model is tailored for a specific class of shapes, namely surfaces of revolution with at most one inflection point on the meridian curve. As demonstrated in our results section, the characterization of equilibrium curves in our method can be easily adjusted to cover this class of shapes, but is also more general.

*Simulation-based* techniques take the mechanical behavior of the material into account, can provide accurate structural insights, or solve for configurations under force equilibrium. Modeling the mechanical behavior of rods has been extensively studied across disciplines. In graphics, simulation of thin solids has been based on Cosserat theory [Pai 2002] and piecewise helices [Bertails et al. 2006] for example. In our work, we employ the discretization suggested by Bergou et al. [2008] for stability analysis and numerical simulation.

Miguel et al. [2016] design sculptures made of bent wire. The rest shape of the wires is optimized to ensure structural stability of the assemblage with only frictional contact between wires. Compliant bent wire structures can also be used to realize kinetic wire characters [Xu et al. 2019]. Perez et al. [2015] numerically optimize the radii and rest shape of flexible rod meshes to match a target shape given boundary conditions. Introducing an interactive design system, He et al. [2019] transform static shapes into deformable objects by customizing the deformation behavior of helical springs. These methods either rely on plastic wire bending or 3d printing for fabrication.

Panetta et al. [2019] propose an optimization-based design method for a grid of elastic beams coupled through rotational joints, which can be deployed into a 3d target shape. Their formulation ensures structural integrity and uses a sparse set of actuation points for deployment. FlexMaps [Malomo et al. 2019] customize the bending and stretching properties of flat, flexible panels so their deformed configuration matches a desired 3d shape after assembly. Combining a pre-stretched sheet with a computer-optimized planar rod network [Pérez et al. 2017], rods arranged in tiled star patterns [Jourdan et al. 2020], or a thin layer of 3d printed tiles [Guseinov et al. 2017] allow these structures to self-deploy into complex 3d surfaces. Guseinov et al. [2020] propose an inverse design tool to encode spatial and temporal morphing of initially flat, self-actuating shells by controlling the softening rate through mesostructure geometry. Xu et al. [2019] optimize for the flat initial configuration of a target structure composed of elastic ribbons using a combination of finite element analysis and a genetic algorithm.

Common to most of these design approaches is that they rely on numerical simulation, define an objective function, and employ nonlinear gradient-based optimization or metaheuristics. In contrast, we first derive a geometric characterization of all mechanically viable shapes. This provides the insights to generate blueprints that are ready for fabrication directly from the target shape, by solving a small linear program. We also show how this method impacts other design stages, like avoiding the costly forward-simulation step in form-finding algorithms, and enabling stability optimization.

Design with bending-active elements also plays an important role in architecture. An excellent overview has been compiled by Lienhard et al. [2013]. In addition to geometric and simulation-based approaches, also experimental, hybrid analogue and digital processes [Symeonidou 2015], or dedicated data-driven models that map knowledge derived from physical form-finding experiments to shapes [Fleischmann and Menges 2011] have been explored.

*Beyond computational fabrication*, there is work on determining the geometry of a rod given its shape when suspended under gravity, with applications to physics-based computer animation. Derouet-Jourdan et al. [2010] compute the material parameters and natural curvature of a plane elastic clamped-free rod that matches a given curve under gravity. They also show that the equilibrium is stable given a large enough stiffness-to-density ratio of the material. Similar in spirit, Bertails-Descoubes et al. [2018] show uniqueness of the natural shape for framed curves in $\mathbb{R}^3$ up to torsion, for clamped-free isotropic Kirchhoff rods under gravity.

In contrast to these works, we classify all plane elastic equilibrium curves that can be achieved from *flat* initial configurations, for the sake of simplifying fabrication. Our main result considers clamped-clamped rods without gravity, but we show how it can be adapted for all common types of boundary conditions, for fixed natural curvature, and to account for gravity as well.

## 2.2 Stability Analysis

Most work treats the stability of *constant-stiffness* elastic curves, such as an early proof that all non-inflectional curves with kinematic boundary conditions are stable [Born 1906, p. 17]. The most comprehensive study notes that, for the constant-stiffness case "it can readily be shown that the higher modes are all unstable. [...] The case of variable stiffness is not so easily treated, and we reach no conclusions." [Maddocks 1981, p. 52]. Recent work examines inflectional curves with different combinations of boundary conditions [Batista 2015; Sachkov and Levyakov 2010]. Only a small number of works treat the variable-stiffness case, for specific load cases and stiffness profiles [Coşkun 2010; Lee and Lee 2018].

The main technical tools for analyzing stability are eigenvalue analysis and the Jacobi criterion [Gelfand and Fomin 1963; Manning et al. 1998]. Gradient-based optimization has been applied to modify eigenvalues before [Bharaj et al. 2015], but we argue in Section 6 that the Jacobi criterion is a much better fit to optimize stability of elastic curves. We thereby avoid solving costly constrained eigenvalue problems and computing their derivatives in every iteration, and replace them with a computation of a matter of milliseconds. This work is the first to derive the adjoint equations of the Jacobi criterion, and to use them in iterative optimization.

# 3 OVERVIEW

We begin our considerations with the variable-stiffness version of the classical Elastica problem: Which plane curves can be obtained as equilibria of slender beams? In Section 4, we show that the main geometric condition is the existence of a line that intersects a curve in its inflection points, and nowhere else. Building on this, we describe a construction process for a stiffness profile that realizes a given equilibrium curve, and which is optimal—in a well-defined sense—for fabrication. Section 5 proposes a modification that lets us incorporate the dead load of a member into this construction process. In Section 6, we turn to the stability of elastic curves and devise an algorithm that turns an unstable curve into a stable one, sometimes by imperceptibly small modifications. We will see that our solution to the variable-stiffness Elastica problem provides the key insight to enable this application. Section 7 gives details about the discretization and implementation of the concepts discussed thus far. In Section 8, we describe and validate the fabrication process behind the physical active-bending models that we present in Section 9, along with rendered examples and quantitative data.

In particular, we consider these our main technical contributions:

- A geometric characterization of all plane elastic curves (Sections 4.2, 4.3, Appendix A);
- A fast and fabrication-friendly construction algorithm for stiffness profiles of elastic curves (Section 4.4);
- An extension of this algorithm that accounts for the dead load of the structural member (Sections 5.1–5.3);
- A derivation of the adjoint equations for the Jacobi stability criterion, and their use in stability optimization of elastic curves (Sections 6.2–6.4, Appendix B);
- Fabrication methods for realizing stiffness profiles as elastic strips (Section 8.1).

# 4 EQUILIBRIUM CURVES

This section treats the most straight-forward adaptation of the Elastica problem to our setting: Characterize the set of plane curves that occur as static equilibria of straight elastic rods. The crucial

difference to the original Elastica problem is that we explicitly allow the stiffness of a rod to vary across its length.

We show that this set of equilibrium curves is characterized by an intuitive geometric property having to do with collinearity of inflection points. In addition, the characterization is computationally convenient and gives rise to an algorithm that finds the "best"—in a well-defined sense—geometry of a rod that matches the desired equilibrium curve.

We first introduce the mathematical model for kinematic elastic rods and arrive at an equilibrium equation. Then, we characterize the set of all curves satisfying this equation with a suitable constitutive law. Finally, we present a linear program that finds the optimal stiffness profile for a desired equilibrium shape, with respect to a manufacturability objective.

## 4.1 Mathematical Model

*Preliminaries.* The deformed state of an inextensible elastic rod in the plane is modeled as a curve $\gamma : [0, l] \to \mathbb{R}^2$, passing through the centerline of the rod. For notational convenience, we assume an arc-length parametrization, i.e., $\|\gamma'\| \equiv 1$. But for a computer implementation of algorithms presented in this paper, any regular parametrization will suffice. We only assume $\gamma \in C^2$, so the signed curvature $\kappa = \det(\gamma', \gamma'')$ is continuous. In addition, denote by $\alpha \in C^1$ the turning angle of $\gamma$, so $\gamma' = (\cos\alpha, \sin\alpha)$ and $\alpha' = \kappa$. The notation used throughout this section is summarized in Fig. 3.

The resistance of a rod to bending is given by a stiffness function $K : [0, l] \to \mathbb{R}_{>0}$, which determines the ratio between curvature and moment of force at any point. E.g., if a linearly elastic rod has a rectangular cross section with width $w$ and thickness $h$ at $s \in [0, l]$, its stiffness will be $K(s) = \frac{1}{12} E w h^3$, where $E$ is the Young's modulus of the material. Most examples presented in this paper will have constant thickness $h$, so the width $w$ scales linearly with $K$. Real materials cannot exhibit stiffnesses that are arbitrarily low or high, which motivates:

**Definition 1.** Let $K : [0, l] \to \mathbb{R}_{>0}$ such that there exist $c, C \in \mathbb{R}$ with $0 < c \le K(s) \le C$ for all $s \in [0, l]$. Then $K$ is called *admissible*.

We will study the design space offered by admissible stiffness functions, because they correspond to elastic rods that we can manufacture in the real world. Note that the existence of a positive lower bound $c$ is a strictly stronger requirement than $K > 0$ and ensures that the ratio between $\sup K$ and $\inf K$ is finite.

*Equilibrium Equation.* Equilibrium configurations of an elastic rod are characterized by extremals of the bending energy $\int \frac{1}{2} K \kappa^2$, subject to boundary conditions and constraints that reflect how the ends of the rod are fixed. We will assume *kinematic* rods, i.e., rods in which $\alpha(0), \gamma(0)$ and $\alpha(l), \gamma(l)$ are all constrained. This leads to a variational problem with Dirichlet boundary conditions and two integral constraints, and we are looking for extremals of

$$W[\alpha] = \int_0^l \frac{1}{2} K (\alpha')^2 \quad \text{s.t.} \quad \begin{matrix} \alpha(0) = \alpha_0, \\ \alpha(l) = \alpha_l, \end{matrix} \quad \text{and} \quad \int_0^l \begin{pmatrix} \cos\alpha \\ \sin\alpha \end{pmatrix} = \gamma_l. \quad (1)$$

The endpoint $\gamma(0)$ is assumed to coincide with the origin, and the endpoint $\gamma(l) = \int_0^l \gamma' = \int_0^l \left(\begin{smallmatrix} \cos\alpha \\ \sin\alpha \end{smallmatrix}\right)$ is constrained to lie at $\gamma_l$.

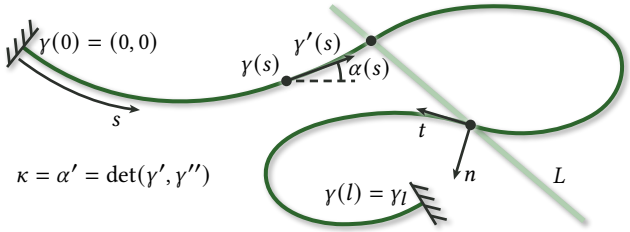


Fig. 3. **Curve Description.** Plane curve $\gamma$ with arc-length parameter $s$, turning angle $\alpha$, signed curvature $\kappa$, and length $l$. The endpoints are the origin and $\gamma_l$. The pair $(t, n)$ forms a right-handed coordinate system adapted to $\gamma$ at an inflection point, and $L$ is a line incident to all inflection points.

The constrained Euler–Lagrange equation of this problem is

$$-(K\kappa)' + \langle \lambda, R\gamma' \rangle = 0, \quad (2)$$

where $R = \left(\begin{smallmatrix} 0 & -1 \\ 1 & 0 \end{smallmatrix}\right)$, and the Lagrange multiplier $\lambda \in \mathbb{R}^2$ needs to be chosen to satisfy the integral constraints. Next, we rename $\lambda = Rb$, which simplifies $\langle \lambda, R\gamma' \rangle = \langle b, \gamma' \rangle$, and integrate the equation through. This adds an integration constant $a \in \mathbb{R}$ and yields the moment equilibrium equation

$$K\kappa = a + \langle b, \gamma \rangle. \quad (3)$$

We characterize curves that satisfy this equation by:

**Definition 2.** Let $\gamma \in C^2([0, l]; \mathbb{R}^2)$ be an arc-length parametrized plane curve with signed curvature $\kappa$. If there exist $a \in \mathbb{R}$, $b \in \mathbb{R}^2$, and an admissible stiffness function $K$ such that $K\kappa = a + \langle b, \gamma \rangle$, then $\gamma$ is called an *equilibrium curve*.

This definition is chosen so a curve $\gamma$ is an equilibrium curve if and only if it is possible to manufacture a straight elastic rod that has $\gamma$ as an equilibrium shape when kinematic boundary conditions are applied. In the next section, we show how the set of all equilibrium curves can be characterized geometrically. This results in a description of the design space of plane kinematic rods that is both intuitive and mathematically sharp.

## 4.2 Characterization of Equilibrium Curves

If $\gamma$ is a line segment, the rod is undeformed, and Eq. 3 is trivially solved by $a = 0$, $b = 0$, and $K$ arbitrary. The theorem below treats the more interesting case, in which the rod undergoes bending. It shows that the main geometric condition for $\gamma$ to be an equilibrium curve is the existence of a line that intersects $\gamma$ exactly in its inflection points (see inset). The only technical assumption we make, apart from $\gamma \in C^2$, is that the number of inflection points be finite, which is a natural expectation in the context of design.

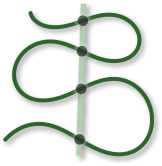

Before we state the theorem, we introduce one more definition:

**Definition 3.** A function $f : \mathbb{R} \to \mathbb{R}$ with $f(x_0) = 0$ is called secant-bounded at $x_0$ if there exist $\varepsilon > 0$ and $m, M \in \mathbb{R}$ with either $m, M > 0$ or $m, M < 0$ such that, for all $h \in (-\varepsilon, \varepsilon)$,

$$\min\{mh, Mh\} \le f(x_0 + h) \le \max\{mh, Mh\}.$$

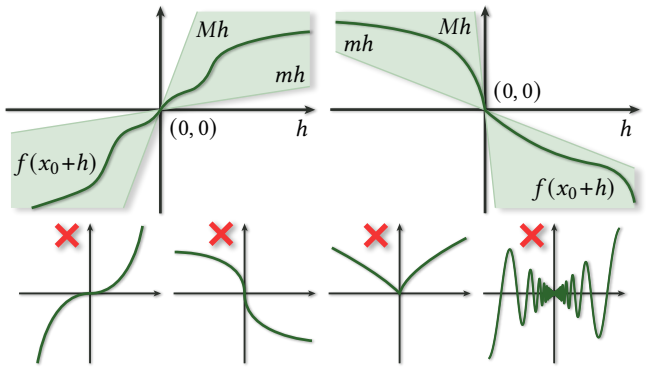


Fig. 4. **Secant-boundedness.** *Top:* A function $f : \mathbb{R} \to \mathbb{R}$ with $f(x_0) = 0$ is secant-bounded at $x_0$ if its graph, restricted to some interval $(x_0 - \varepsilon, x_0 + \varepsilon)$, is contained in a double cone that is bounded by two linear functions $mh$ and $Mh$, where either $m, M > 0$ *(left)* or $m, M < 0$ *(right). Bottom:* Examples of functions that fail to be secant-bounded at the origin.

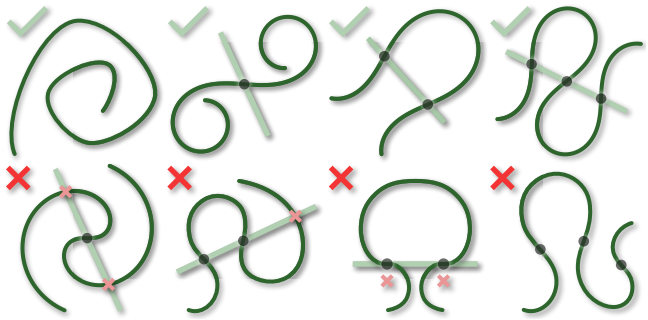

Fig. 5. **(Non-)Equilibrium Curves.** *Top:* Four equilibrium curves, from a non-inflectional curve *(left)* to a curve with three inflections *(right). Bottom:* Four curves that are not equilibrium curves because *(from left to right)* every line through the inflection intersects the curve in further points; the unique inflection line intersects the curve in a non-inflectional point; the inflection line is tangent to the curve; the inflection points are not collinear.

Fig. 4 illustrates secant-boundedness and gives examples of functions that do not have this property.[1] Now we are ready to state our main theoretical result, which is proved in Appendix A:

**Theorem 1.** *Let $\gamma \in C^2([0,l];\mathbb{R}^2)$ be an arc-length parametrized plane curve with signed curvature $\kappa = \det(\gamma', \gamma'')$, and the set of zero-curvature parameters $S_0 := \{s \in [0,l] : \kappa(s) = 0\}$ finite. Then, $\gamma$ is an equilibrium curve if and only if*

(1) *there exists a line $L$ that intersects $\gamma$ exactly in its zero-curvature points, and that is not tangent to $\gamma$ in any of these intersections;*
(2) *$\kappa$ is secant-bounded at every $s_0 \in S_0$.*

*Remark* 1. The secant-boundedness of $\kappa$ on $S_0$ implies that $\kappa$ actually changes sign at every root; but it is even stronger, as seen in Fig. 4 (bottom). In case $\kappa \in C^1$, the condition reduces to $\kappa'(s_0) \neq 0$.

*Remark* 2. In the context of design, condition (2) may seem overly technical to be of practical relevance. However, in Section 6, we will see that this condition is computationally significant because it causes an algorithm to fail unless explicitly enforced.

### 4.3 Properties of Equilibrium Curves

The geometric characterization given above is intuitive enough that we can usually tell by inspection whether a curve is an equilibrium curve. The main condition is that all inflection points lie on a line which does not cross the curve in non-inflectional points. In particular, this means that every curve without inflections is an equilibrium curve. For curves with at least one inflection, it depends on the global shape whether it has the equilibrium property, as shown by example in Fig. 5. We can infer some more properties that are useful in a design context:

**Locality.** Every curve that satisfies the technical requirements of Theorem 1 is locally an equilibrium curve, i.e., it can be split into a finite number of equilibrium curves. Thus, every curve can be realized with an elastic rod if we introduce additional fixed points.

**Projective invariance.** The class of equilibrium curves is closed under projective transformations. This holds because collinearity of inflection points is a projective invariant. It is thus possible to create new equilibrium curves by editing an existing curve with projective transformation tools.

**Smoothness of $K$.** The smoothness of the stiffness function will affect the visual appearance of a manufactured rod, and may thus be of interest. If $\gamma \in C^r$, we infer from $K = \frac{a+\langle b,\gamma\rangle}{\kappa}$ that $K$ is at least $C^{r-2}$ away from inflection points, and at least $C^{r-3}$ at inflection points. E.g., to ensure that $K$ is continuous in a design with inflections, one may use quartic splines, so $\gamma \in C^3$. Without inflections, cubic splines suffice.

The applicability of Theorem 1 can be expanded by considering the following variants, which can be proved in the same way as the original statement:

**Boundary conditions.** Theorem 1 assumes kinematic boundary conditions to maximize the design space, but we can account for the effect of removing positional or angle constraints by imposing additional requirements on $\gamma$ and $L$. If the endpoint constraint on $x$ ($y$) is removed, this constrains $L$ to be vertical (horizontal). If both are removed, $\gamma$ must not have inflections. If the angle constraint at either endpoint is removed, the curvature of $\gamma$ needs to vanish at this endpoint, which in turn requires $L$ to intersect it.

**Fixed natural curvature.** By substituting every occurrence of "$\kappa$" in Theorem 1 with "$\kappa - \kappa_0$", we can also characterize the equilibrium curves of plane rods with fixed natural curvature $\kappa_0$.

### 4.4 Computation of Stiffness Profiles

To synthesize the geometry of a rod, it suffices to prescribe its stiffness at every $s \in [0,l]$. The stiffness can then be transformed into a cross section, e.g., a rectangular cross section with width $w$ and thickness $h$, such that $K$ is proportional to $wh^3$ everywhere.

The stiffness function of an equilibrium curve is not generally unique, because it depends on the choice of $a \in \mathbb{R}$ and $b \in \mathbb{R}^2$ via

[1] Note that secant-boundedness is weaker than being locally bi-Lipschitz at $x_0$, which is defined as follows: there exist $\varepsilon, L > 0$ such that for all $x, y \in (x_0 - \varepsilon, x_0 + \varepsilon)$, it holds that $|x - y|/L \leq |f(x) - f(y)| \leq L|x - y|$. In particular, locally bi-Lipschitz functions are locally injective—secant-bounded functions need not be.

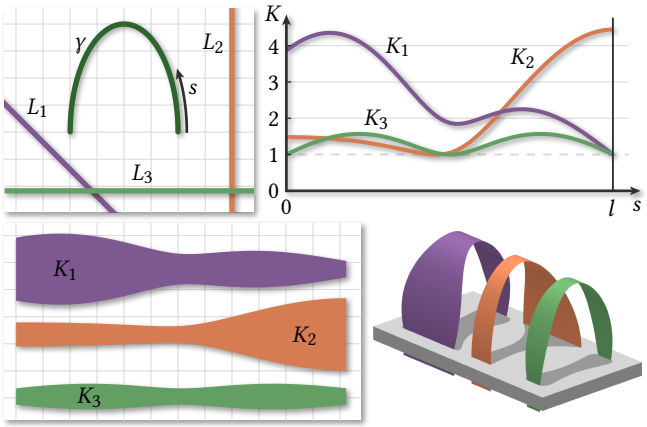


Fig. 6. **Stiffness Profiles.** *Top left:* An elliptical arc $\gamma$ and three lines representing viable choices of $a, b$. *Top right:* Stiffness profiles induced by the lines; $K_3$ was computed using Eq. 4 and minimizes $R$ globally. *Bottom left:* Outlines of elastic strips realizing the stiffness profiles. *Bottom right:* Deformed rods with boundary conditions applied, yielding identical shapes.

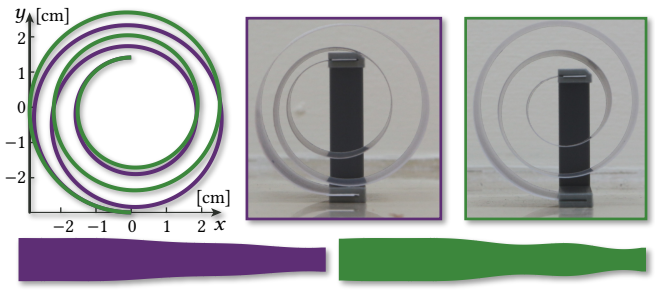


Fig. 7. **Spiral under Gravity.** *Top:* Target curve (green) and predicted shape if gravity is neglected in the linear program (purple); physical models, computed with Eq. 4 *(center)*, and with Eq. 6 *(right). Bottom:* Shapes of the elastic strips cut from cardboard.

$K = \frac{a+\langle b,\gamma\rangle}{\kappa}$. For curves with two or more inflections, $L$ is unique and thus defines $a$ and $b$ up to scalar multiples. But for curves with zero or one inflection, additional degrees of freedom remain. This raises the question of what the "best" stiffness function is, and how it can be computed. In a fabrication setting, one is typically limited by the range of stiffnesses that can be reliably achieved within a single structural element. Thus, in our view, the best stiffness function is the one that minimizes the max-to-min stiffness ratio $R[K] := \frac{\sup K}{\inf K}$.

To find the global minimizer of $R$, note that $R$ is naturally scale-invariant: If $K$ is an admissible stiffness for $\gamma$, so is $\theta K$ for any $\theta > 0$. Likewise, if $K$ is a minimizer of $R$, so is $\theta K$. This means that we can eliminate scalar multiples without losing any solutions, for example by imposing the affine constraint $\inf K = 1$. In the affine subspace defined by this constraint, the objective simplifies to $R[K] = \sup K$, which shows that the problem of minimizing $R$ is in fact linear, and can be discretized using a linear program.

To do this, let $S_0 = \{s_1^{\text{infl}}, \dots, s_m^{\text{infl}}\}$, and $0 = s_1, \dots, s_n = l$ a sampling of $[0, l]$ that does not include any of the inflection points in $S_0$. The sampling should be dense enough so $\max\{K(s_1), \dots, K(s_n)\}$ approximates $\sup K$ well. Then, solve the following linear program in the variables $a, R \in \mathbb{R}$ and $b \in \mathbb{R}^2$:

$$\begin{aligned} &\text{minimize } R, \\ &\text{subject to } 1 \le \frac{a + \langle b, \gamma(s_i)\rangle}{\kappa(s_i)} \le R, && i = 1, \dots, n, \qquad (4) \\ &\qquad 0 = a + \langle b, \gamma(s_i^{\text{infl}})\rangle, && i = 1, \dots, m. \end{aligned}$$

The fraction appearing in the linear program equals $K(s_i)$, and $\min_i K(s_i) = 1$ is implicitly enforced by the inequality constraints $1 \le K(s_i)$. The equality constraints ensure that $L$ intersects all inflection points of the curve. Furthermore, it is guaranteed that $L$ does not intersect the curve in non-inflectional points, because this would result in a negative stiffness value at a sample adjacent to the intersection. With only four variables and $2n+m$ constraints, this linear program is very small and can be solved almost instantaneously for arbitrary curves.

Fig. 6 shows how the stiffness profile for a curve varies with the choice of $a$ and $b$. An arbitrary choice may result in unwieldy rod geometries such as $K_1$ and $K_2$. The profile $K_3$, which is the global minimizer of $R[K]$, was found by solving the linear program.

## 5 EQUILIBRIUM CURVES UNDER GRAVITY

The theory presented in the previous section suffices to create designs on a scale where the effect of gravity is negligible. For applications in which the dead load of a beam significantly affects the equilibrium shape, like the one shown in Fig. 7, we need to model gravity explicitly. Although we cannot use Theorem 1 to determine feasibility in this case, we show that it is possible to adapt the computation of stiffness profiles to account for gravity exactly.

The main finding is that the problem of determining feasibility and finding the "best" stiffness profile under gravity remains linear if the thickness of the material is known a priori. Furthermore, the complexity of the linear program used to solve it only increases marginally, and solutions can still be found near instantaneously.

### 5.1 Mathematical Model

The gravity potential of a body $V \subset \mathbb{R}^3$ with density $\rho$ in the earth's gravitational field is given by $U = \int_V \rho(x)\langle x, g\rangle \mathrm{d}x$, with $g$ the gravitational acceleration vector. For an elastic strip with constant thickness $h$ and variable width $w$, we can write this integral as $U = \int_0^l \rho h w(s)\langle\gamma(s), g\rangle \mathrm{d}s$. We can also express the stiffness in terms of these quantities, which yields $K = \frac{1}{12}Ewh^3$, with $E$ the Young's modulus of the material. Substituting $w$ for $K$ and summing gravity potential and bending energy gives the functional

$$W[\alpha] = \int_0^l K\left(\frac{1}{2}\kappa^2 + \langle\gamma, e\rangle\right) \quad \text{with } e = \frac{1}{\beta l^3}\cdot\frac{g}{\|g\|}, \quad \beta = \frac{Eh^2}{12\rho\|g\|l^3},$$

where $\beta$ is the standard gravito-bending parameter [Audoly and Pomeau 2010, 4.1.2]. We estimate this parameter by cutting a rectangular strip of a material, and measuring the displacement in a cantilever experiment. Then, we fit the parameter so the minimizer

of $W$ matches the observed displacement. For 200 gsm cardboard, we found $\beta l^3 = 8.86 \cdot 10^{-4}\mathrm{m}^3$, which we use for all examples.

The appearance of $\gamma(s) = \int_0^s \binom{\cos\alpha}{\sin\alpha}$ in the energy means that $W$ depends on $\alpha$ via a double integral. To find the Euler–Lagrange equation of a functional like this, we compute the variational derivative with respect to $\alpha$, and then test against a delta-distribution centered at $s$, as detailed in the supplemental document. This gives

$$-(K\kappa)'(s) + \langle b, \gamma'(s)\rangle + \langle R^t e, \gamma'(s)\rangle \int_s^l K(t)\,\mathrm{d}t = 0,$$

where $R = \left(\begin{smallmatrix} 0 & -1 \\ 1 & 0 \end{smallmatrix}\right)$. This equation can be integrated to yield the moment equilibrium equation

$$\begin{aligned} -K(s)\kappa(s) + \langle b, \gamma(s)\rangle + \langle R^t e, \gamma(s)\rangle \int_s^l K(t)\,\mathrm{d}t \\ - \int_s^l \langle R^t e, \gamma(t)\rangle K(t)\,\mathrm{d}t + a = 0. \end{aligned} \tag{5}$$

A comparison with Eq. 3 shows that two new summands involving integrals have appeared due to the effect of gravity. Below, we show how to account for them in the computation of stiffness profiles.

## 5.2 Computation of Stiffness Profiles

In Eq. 5, the stiffness $K$ appears in three different forms: evaluated at $s$, integrated from $s$ to $l$, and once more integrated against $\langle R^t e, \gamma\rangle$. All three appearances are linear in $K$, so we can still cast this as a linear program.

To do this, let $0 = s_1, \ldots, s_n = l$ be a dense sampling of $[0, l]$. Associate with the samples a set of weights $w_1, \ldots, w_n$ based on the Voronoi lengths of the samples along the curve, so $\int_{s_k}^{s_n} f \approx \sum_{i=k}^n w_i f(s_i)$. In addition to $a, R \in \mathbb{R}$ and $b \in \mathbb{R}^2$, the linear program has auxiliary variables for $K$, and for the two types of integrals that appear in Eq. 5, call them $F$ and $G$. Then, the program is given by

$$\begin{aligned} &\text{minimize } R, \\ &\text{subject to } 1 \le K_i \le R, && i = 1, \ldots, n, \\ &\qquad 0 = -K_i\kappa(s_i) + \langle b, \gamma(s_i)\rangle \\ &\qquad\quad + \langle R^t e, \gamma(s_i)\rangle F_i - G_i + a, && i = 1, \ldots, n, \\ &\qquad F_i = F_{i+1} + w_i K_i, && i = 1, \ldots, n, \\ &\qquad G_i = G_{i+1} + w_i \langle R^t e, \gamma(s_i)\rangle K_i, && i = 1, \ldots, n, \end{aligned} \tag{6}$$

where we set $F_{n+1} = 0 = G_{n+1}$. The last two lines constrain $F_i \approx \int_{s_i}^l K$ and $G_i \approx \int_{s_i}^l \langle R^t e, \gamma\rangle K$. In total, the program has $3n + 4$ variables, $2n$ inequality constraints, and $3n$ equality constraints. It is possible to eliminate the variables $F_i$, $G_i$ and their defining equality constraints by substitution. But even in its stated form, the program can be solved to optimality within a few milliseconds for any curve.

Fig. 7 shows a challenging example, in which precise estimation of the gravity parameter $e$ is paramount. The influence on the stiffness profile is subtle, but shape reproduction is significantly improved: Neglecting gravity yields a model that sags under gravity and collides with the support structure; taking gravity into account explicitly results in a uniform spiral that is only supported at the endpoints.

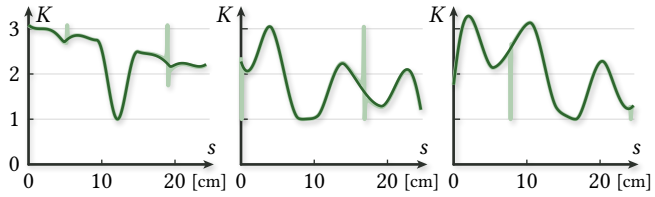


Fig. 8. **Inflectional Curves under Gravity.** Stiffness functions after solving Eq. 6 (light green) and after solving the modified linear program (dark green) for curves taken from the flower pot example, see Fig. 19.

## 5.3 Inflectional Curves

If admissible stiffness profiles exist for a given curve, Eq. 6 always finds the one that minimizes $R$. However, this minimizer is sometimes surprisingly noisy near inflection points, which is a byproduct of curve discretization. In particular, $K$ tends to have spikes like the ones shown in Fig. 8 (light green), which allow for a small decrease in $R$ compared to a more preferable, smooth solution.[2] To remove these spikes, and still retain a solution to Eq. 5, we solve a second linear program that is obtained from Eq. 6 by two modifications:

- Replace the objective function by a discretization of $\mathrm{V}(K') = \int_0^l |K''|$, the total variation of $K'$.
- Add the constraint $R \le R_1 \cdot (1 + \varepsilon)$, where $R_1$ is the optimal value obtained from solving Eq. 6. We always set $\varepsilon = 0.01$.

The new objective function favors solutions without noise, and the original optimum is retained up to a margin of $\varepsilon$. This new linear program is feasible whenever the original problem is feasible, because the optimal point of Eq. 6 is feasible in the new program. We have used this two-phase optimization in every example that treats inflectional curves under gravity, and it has yielded completely noise-free results in every case, like the examples in Fig. 8.

# 6 STABILITY OF EQUILIBRIUM CURVES

A solution to a variational problem is said to be stable if it is a local minimum of the energy functional. Unstable solutions are saddle points, which means that there is a perturbation of the solution, compatible with boundary conditions and constraints, that attains lower energy. For a physical system, this means that force equilibrium holds at a saddle point, but any disturbance will cause it to become dynamic, rendering it useless for most applications.

*Overview.* From visual inspection alone, it is far from obvious whether a specific equilibrium curve will be stable, or even whether there could be a *similar* equilibrium curve that is stable. The remainder of this section describes an optimization algorithm that, given an unstable equilibrium curve, finds a similar equilibrium curve which is stable. We believe this is the first algorithm of this type.

Our method is based on the theory of isoperimetric conjugate points, which we review below. Then, we present our idea for stability recovery, based on applying the adjoint method to the isoperimetric Jacobi equations. Before discussing our final algorithm, we

[2] Note that this only happens when gravity is taken into account. In contrast, solutions to Eq. 4 are always noise-free, regardless of inflections, because the inflection line is sufficiently constrained by the equation $0 = a + \langle b, \gamma(s_i^{\mathrm{infl}})\rangle$.

outline why a simpler and more obvious version of the algorithm fails. Theorem 1 plays a crucial role in formulating the method, so it is currently limited to applications in which gravity is negligible.

### 6.1 Stability Criteria

There are two essential procedures for analyzing the stability of a solution to an optimization problem: the eigenvalue test and the Jacobi test. The eigenvalue test is used more frequently in practice, but we will argue that the Jacobi test is better suited to the problem at hand and leads to an elegant optimization algorithm at a low computational cost.

*The Eigenvalue Condition.* A sufficient criterion for stability is the positivity of all eigenvalues of the energy Hessian. For constrained problems, there exists a similar criterion involving eigenvalues of directions constrained to the orthogonal subspace of constraint tangents. This method is very general, but it does not take advantage of the structure inherited from continuous variational problems.

There are two obstacles to using the eigenvalue method for optimizing stability of kinematic elastic curves. First, such optimizations are iterative, and require solving a constrained eigenvalue problem at every step. These computations are very costly because standard numerical packages such as LAPACK do not support solution procedures that preserve sparsity for this case. Second, unlike the unconstrained case [Van der Aa et al. 2007], we have found no reference on computing derivatives for constrained eigenvalue problems.

*The Jacobi Condition.* A different stability criterion can be derived directly from the continuous variational problem, and then discretized. This condition, named after Jacobi, can be checked by integrating simple initial-value problems on $[0, l]$. The result regarding stability is equivalent to that of the eigenvalue test, despite a significantly lower computational cost, and a complexity that is only linear in the number of samples. In addition, the criterion we use for establishing stability is differentiable via the adjoint method, and not subject to singularities that might be present in the eigenvalue structure. Below, we review a version of the Jacobi condition that allows for multiple equality constraints [Manning et al. 1998].

### 6.2 Isoperimetric Conjugate Points

*General Theory.* In this section, we summarize the sufficient stability criterion for constrained variational problems based on conjugate points, omitting derivations. We start with a sufficiently regular functional $J[u] = \int_0^l f(x, u(x), u'(x))\,\mathrm{d}x$ subject to Dirichlet b.c., and integral constraints $\int_0^l g_i(u(x))\,\mathrm{d}x = c_i$, for $i = 1, \dots, p$. Then, the Lagrangian of the problem is given by $\mathcal{L}[u] = \int_0^l f^*(x, u, u')\,\mathrm{d}x$, where $f^* = f + \sum_i \lambda_i g_i$. The Lagrangian can be developed into a second-order Taylor series as

$$\mathcal{L}[u+h] = \mathcal{L}[u] + \int_0^l \left(f_u^* - \frac{\mathrm{d}}{\mathrm{d}x} f_{u'}^*\right) h + \frac{1}{2}\int_0^l \left(P h'^2 + Q h^2\right) + o(\|h\|_w^2),$$

$$\text{with} \quad P = f_{u'u'}^*, \quad Q = f_{uu}^* - \frac{\mathrm{d}}{\mathrm{d}x} f_{uu'}^*, \quad \|h\|_w^2 = \|h\|_{L^2}^2 + \|h'\|_{L^2}^2.$$

In analogy to minimization problems with finite dimension, $J$ has a constrained minimum at $u$ if the first-order term in the expansion of $\mathcal{L}$ vanishes, and the second-order term is positive-definite within the orthogonal subspace of constraint tangents. The first-order condition is exactly the constrained Euler–Lagrange equation. Positive-definiteness of the second-order term is guaranteed if the so-called Legendre and Jacobi conditions are satisfied. The Legendre condition is met if $P > 0$ everywhere.

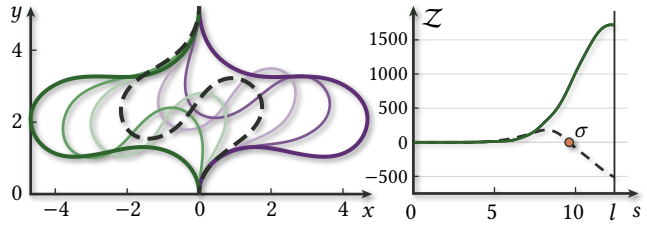


Fig. 9. **Stability and Conjugate Points.** *Left:* Unstable equilibrium (dashed), two stable equilibria (green, purple), and in-between non-equilibrium states of the same rod. *Right:* Stability determinant $\mathcal{Z}(s)$ for unstable and stable equilibria, with $\sigma$ marked (orange).

For the Jacobi condition, we need the concept of isoperimetric conjugate points. First, let $\zeta$ be the solution to the *Jacobi equation*,

$$-(P\zeta')' + Q\zeta = 0 \quad \text{s.t.} \quad \zeta(0) = 0,\ \zeta'(0) = 1,$$

and let $\eta_i$, for $i = 1, \dots, p$, be the solutions to

$$-(P\eta_i')' + Q\eta_i = T_i \quad \text{s.t.} \quad \eta_i(0) = 0,\ \eta_i'(0) = 1,$$

where $T_i := \mathrm{d}g_i/\mathrm{d}u$ are the constraint tangents. Next, we define the running integrals

$$M_i(x) = \int_0^x T_i\zeta \quad \text{and} \quad N_{ij}(x) = \int_0^x T_i\eta_j \quad \text{for} \quad i, j = 1, \dots, p.$$

This gives the entries of the *constrained stability matrix*,

$$Z(x) = \begin{pmatrix} \zeta(x) & \eta_1(x) & \cdots & \eta_p(x) \\ M_1(x) & N_{11}(x) & \cdots & N_{1p}(x) \\ \vdots & \vdots & \ddots & \vdots \\ M_p(x) & N_{p1}(x) & \cdots & N_{pp}(x) \end{pmatrix}.$$

Finally, let $\mathcal{Z}(x) := \det Z(x)$. A point $\sigma \in \mathbb{R}$ with $\mathcal{Z}(\sigma) = 0$ is called an *(isoperimetric) conjugate point.* The Jacobi condition is satisfied if there is no conjugate point in $(0, l]$.

In summary: If, at $u$, the Euler–Lagrange equation is satisfied, and $P(x) > 0$ for all $x \in [0, l]$, and there is no conjugate point in $(0, l]$, then $u$ is a minimizer.

*Elastic Rods.* Now, we apply this theory to kinematic elastic rods, to determine whether an equilibrium curve $\gamma$ is stable. Stability is mostly an issue for curves with at least two inflection points, so $K$ and $\lambda$ (see Eq. 2) are uniquely determined by $\gamma$ up to positive multiples. Using the variable names from above, we have

$$g_1(\alpha) = \cos\alpha,\ g_2(\alpha) = \sin\alpha, \quad T_1(\alpha) = -\sin\alpha,\ T_2(\alpha) = \cos\alpha,$$
$$P = K, \quad Q = -\lambda_1\cos\alpha - \lambda_2\sin\alpha = -\langle\lambda, \gamma'\rangle,$$

so the Legendre condition $P = K > 0$ is always satisfied. The Jacobi equation reads

$$-(K\zeta')' - \langle\lambda, \gamma'\rangle\zeta = 0 \quad \text{s.t.} \quad \zeta(0) = 0,\ \zeta'(0) = 1, \tag{7}$$

and is readily solved by integrating it from $s = 0$ to $l$. The functions $\eta_1$ and $\eta_2$ are determined by solving with the right-hand sides $T_1$ and $T_2$, respectively. Finally, $M_1$, $M_2$, $N_{11}$, $N_{12}$, $N_{21}$, and $N_{22}$ are obtained by integrating the solutions against the constraint tangents. This gives all entries in the 3-by-3 stability matrix $Z$, whose determinant $\mathcal{Z}$ can be checked for zero-crossings on $(0, l]$. If the sign of $\mathcal{Z}$ remains constant on this interval, then $\gamma$ is a stable equilibrium curve, and otherwise it is unstable. Fig. 9 shows how $\mathcal{Z}$ differs between an unstable and a stable equilibrium of the same elastic rod.

If an equilibrium curve is unstable, the location of the first isoperimetric conjugate point $\sigma \in (0, l]$ indicates how close the curve is to being stable—if $\sigma$ is close to $l$, then the curve is "almost" stable. (This is analogous to the magnitude of the lowest negative eigenvalue.) Our goal is to make a curve stable by pushing $\sigma$ towards $l$, and finally out of the interval $(0, l]$, while modifying the curve as little as possible.

*Adjoint Method.* The function $\mathcal{Z}(s)$ depends on $K$ via the Euler–Lagrange and Jacobi equations, so we write it as $\mathcal{Z}(s, K)$. A conjugate point is implicitly defined via $\mathcal{Z}(\sigma, K) = 0$. We can apply the implicit function theorem to find

$$-\partial\mathcal{Z}/\partial s|_{(\sigma,K)} \cdot \mathrm{d}\sigma/\mathrm{d}K = \partial\mathcal{Z}/\partial K|_{(\sigma,K)}.$$

If we can numerically compute $\mathrm{d}\sigma/\mathrm{d}K$, this gives us a way to apply gradient-based optimization on $K$ in order to push $\sigma$ towards $l$. But the equation shows that $\mathrm{d}\sigma/\mathrm{d}K$ coincides with $\partial\mathcal{Z}/\partial K|_{(\sigma,K)}$ up to a scaling factor $-\partial\mathcal{Z}/\partial s|_{(\sigma,K)}$, which can be shown to always be positive. Because $\mathcal{Z}$ depends on $K$ via a series of differential equations and integrals, we need to derive its adjoint equations in order to compute $\partial\mathcal{Z}/\partial K|_{(\sigma,K)}$ analytically. A full overview of these equations can be found in Appendix B, and a derivation in the supplemental document.

The result of solving the adjoint equations is a differential that lets us evaluate the first-order change to a conjugate point $\sigma$ implied by changing $K$, up to a proportionality factor:

$$\sigma[K + \delta K] \approx \sigma[K] + \delta\sigma[\delta K] = \sigma[K] + \delta F[\delta K]/(-\partial\mathcal{Z}/\partial s|_{(\sigma,K)}).$$

This differential, which we call $\delta F$, can be used to compute a search direction to increase $\sigma$ in an optimization algorithm.

**ALGORITHM 1:** Failed Attempt at Stability Recovery

**Input :** equilibrium curve $\gamma^0$ with stiffness $K^0$ and Lagrange multipliers $\lambda^0$, step size $h$
**Output :** a stable equilibrium curve $\gamma^n$
$n \leftarrow 0$;
**while** $\gamma^n$ *unstable* **do**
  Compute $\mathcal{Z}, \sigma$;
  Compute $\nabla F$ via adjoint method;
  $K^{n+1} \leftarrow K^n + h \cdot \nabla F$;
  Compute $\gamma^{n+1}, \lambda^{n+1}$ based on $K^{n+1}$, with $\gamma^n, \lambda^n$ as initial guess;
  $n \leftarrow n + 1$;
**end**

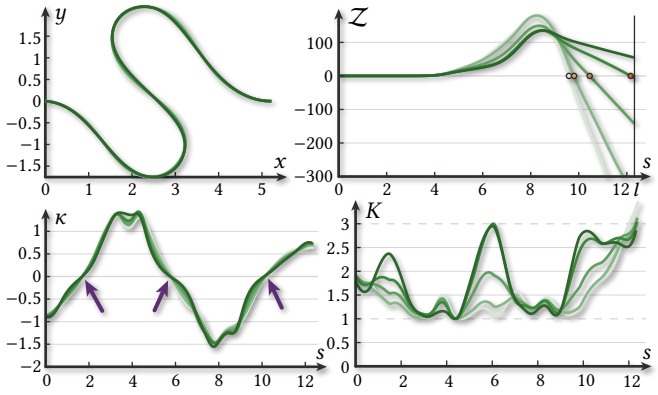


Fig. 10. **Stability Optimization.** Iterations of stability optimization, from initial unstable state (light green) to stable state (dark green). Changes to $\gamma$ *(top left)* are almost imperceptible, but its curvature *(bottom left)* changes visibly around inflection points (arrows). This causes stronger stiffness variations *(bottom right)* and pushes the conjugate point (orange) out of $(0, l]$ *(top right)*. Iterations 0, 8, 15, 23, 30 shown.

## 6.3 A Failed Attempt at Stability Recovery

The most obvious way of using $\delta F$ is to parametrize $K$ by densely sampling it, and assigning one parameter $K_i$ per sample. With this finite parametrization, $\delta F$ gives the gradient $\nabla F$ with respect to $K_i$, which can be used for "steepest ascent" on $\sigma$. The data flow of this algorithm is

$$K \mapsto (\gamma, \lambda) \mapsto (\mathcal{Z}, \sigma) \mapsto F.$$

Algorithm 1, which outlines this idea, makes initial progress in moving $\sigma$ closer to $l$, but necessarily fails to cross the stability threshold. The reason is the bifurcation that occurs between unstable and stable equilibria at $\sigma = l$. At this point, the curve becomes "uncontrollable" through $K$, meaning that small changes to $K$ may induce arbitrarily large changes to $\gamma$, and $\gamma$ may not even be (locally) uniquely defined by $K$. The consequence is that Newton-type methods that compute $\gamma$ from $K$ diverge, and even if they are stabilized, any similarity of $\gamma$ to the original curve is lost in the process.

Theorem 1 offers the tools to tackle the stability optimization problem with a more successful approach: It describes the exact requirements on $\gamma$ under which the inverse map $\gamma \mapsto K$ exists. This map is well-behaved even through bifurcations, and we will use it to construct a working algorithm for stability recovery below.

## 6.4 The Stability Recovery Algorithm

The key to repairing the stability recovery algorithm is to avoid the "forward simulation" step, in which $\gamma$ is computed from $K$. To do this, we exchange the primary variables of the optimization problem, and parametrize $\gamma$ instead of $K$. We opt for a B-Spline representation of at least quartic order, and use the control point coordinates $q \in \mathbb{R}^{2m}$ as parameters to optimize, with $m$ the number of control points. The data flow of the new algorithm is

$$q \mapsto \gamma \overset{!}{\mapsto} (K, \lambda) \mapsto (\mathcal{Z}, \sigma) \mapsto F.$$

The step marked by "!" is only well-defined if $\gamma$ is an equilibrium curve, because otherwise, an admissible stiffness function $K$ does not

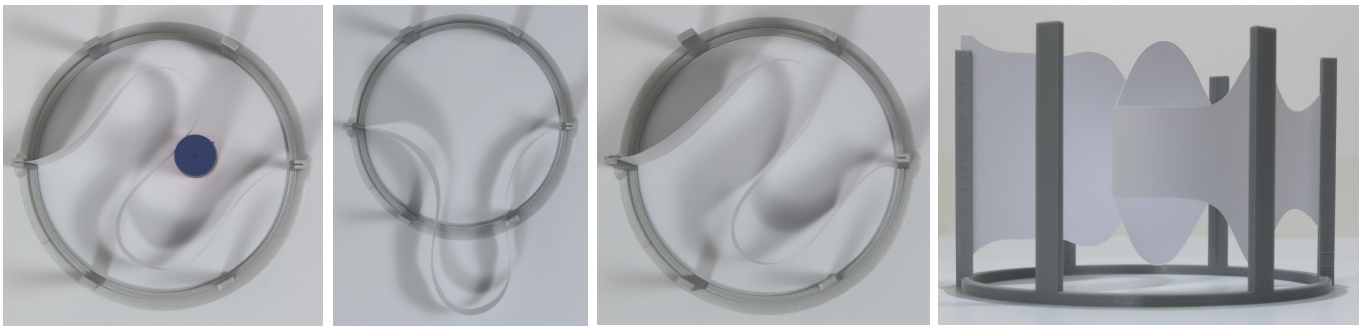

Fig. 11. **Stabilized *S*-curve.** *From left to right:* Initial curve is kept in its unstable equilibrium state by a little friction; initial curve snaps into stable equilibrium once friction is removed; optimized curve is stable in *S*-shape; side view of stable *S*-shape.

exist. This shows the significance of Theorem 1—it gives necessary and sufficient conditions that we can enforce computationally in order to retain the equilibrium property of $\gamma$.

In practice, this means enforcing conditions (1) and (2) of Theorem 1 throughout optimization. The collinearity of inflection points can be formulated as a non-linear equality constraint on $q$, and is enforced via an underdetermined Newton procedure after every update $q \leftarrow q + \Delta q$. This step is also used to enforce other constraints, such as keeping endpoints and tangents fixed, and fixing the arc length of the curve. We describe this procedure in Appendix C.

At this stage, the algorithm converges for some examples, but fails for others. The reason for failure is that the optimization often drives $\gamma$ towards a state in which the secant-boundedness of $\kappa$ is violated, i.e., with $\kappa'(s_0) \approx 0$ at an inflection point $s_0$, as seen in the inset. The easiest way to remedy this, and safeguard against other violations of (1) and (2), is to add a constraint that bounds $R[K] = \frac{\sup K}{\inf K}$ from above. The upper bound $R_{\max}$ can be chosen to reflect the limitations of the fabrication method, or other requirements on the geometry of the rod. This is a single non-linear inequality constraint, and it can be enforced by linearizing the constraint in $q$ and projecting $\Delta q$ onto the tangent space of the constraint boundary, if it violates the constraint to first order. We have found that it is not necessary to iteratively project $q$ back onto the (non-linear) constraint boundary, because violations of $R \leq R_{\max}$ due to the linearization are typically small and temporary if the step size is kept small enough. Algorithm 2 summarizes all steps of computation.

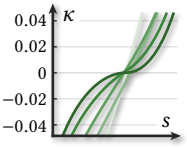


**ALGORITHM 2:** Stability Recovery

**Input** : equilibrium curve $\gamma^0$, step size $h$, stiffness ratio bound $R_{\max}$
**Output**: a stable equilibrium curve $\gamma^n$

$n \leftarrow 0$;
**while** $\gamma^n$ *unstable* **do**
  Compute $a \in \mathbb{R}, b \in \mathbb{R}^2$ from inflection line;
  $K \leftarrow \frac{a+\langle b, \gamma^n \rangle}{\kappa}$; $R \leftarrow \frac{\sup K}{\inf K}$;
  Compute $\mathcal{Z}, \sigma$;
  Compute $\delta F / \delta K$ via adjoint method;
  Compute $\mathrm{d}K/\mathrm{d}q$ and $\mathrm{d}R/\mathrm{d}K$ via chain rule;
  $\nabla F \leftarrow \delta F/\delta K \cdot \mathrm{d}K/\mathrm{d}q$; $\nabla R \leftarrow \mathrm{d}R/\mathrm{d}K \cdot \mathrm{d}K/\mathrm{d}q$;
  $\Delta q \leftarrow h \cdot \nabla F$;
  // Project $\Delta q$ so $R \leq R_{\max}$ is satisfied to first order
  $\Delta q^{\text{eff}} \leftarrow \textsc{ProjectStep}(q, \Delta q, R, \nabla R, R_{\max})$;
  $q \leftarrow q + \Delta q^{\text{eff}}$;
  $q \leftarrow \textsc{EnforceConstraints}(q)$; // Make inflections collinear, enforce b.c.
  $\gamma^{n+1} \leftarrow \textsc{BSpline}(q)$; $n \leftarrow n + 1$;
**end**

*Example.* Fig. 10 shows iterations of optimizing the stability of a quartic spline curve with three inflections, where $R_{\max} = 3$. Remarkably, the curve itself changes very little during optimization, but the stiffness profile implied by the curve changes drastically. This is possible because curvature changes close to inflection points are amplified by the computation $K = \frac{a+\langle b, \gamma \rangle}{\kappa}$.

The first two photos in Fig. 11 show a physical model of the unstable elastic curve, which can be kept in unstable equilibrium with a small amount of force, but otherwise snaps into one of the stable equilibria. The last two photos show a model of the stabilized curve, whose equilibrium shape is almost identical to the unstable one. Note that the model does not touch the ground, so no frictional force is provided. The supplemental video demonstrates the qualitative difference between the two models in motion.

*Remarks.* There are two technical details that we have brushed over so far. First, instead of using $R[K] = \frac{\sup K}{\inf K}$ directly, we replace it by the differentiable approximation $R[K] \approx \|K\|_p \cdot \|1/K\|_p$, with $\|f\|_p = (\int |f|^p)^{1/p}$ and $p$ large; $p > 20$ worked well in our examples.

Second, we did not carefully discuss differentiability of $\gamma \mapsto (K, \lambda)$. This map is only defined on the manifold $\mathcal{M} \subset \mathbb{R}^{2m}$ corresponding to control point coordinates $q$ such that $\gamma$ has collinear inflections. Thus, the domain of the differential is the tangent space $T_q\mathcal{M}$, and not all of $\mathbb{R}^{2m}$. In our implementation, we account for this by computing an explicit basis of $T_q\mathcal{M}$ after enforcing constraints, and performing all subsequent calculations within this subspace.

A current limitation of the stabilization algorithm is that it neglects gravity because it uses Theorem 1 to formulate constraints. Heuristically, we can account for gravity by enforcing Eq. 5 after stabilization while changing $K$ minimally, but this gives no formal stability guarantee.

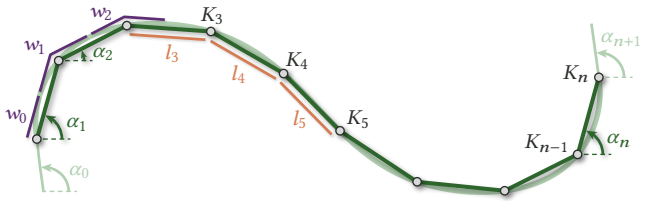


Fig. 12. **Discretization.** Quantities used in the discretization of the bending energy: edge and boundary angles (green), edge weights (orange), nodal stiffnesses (gray), nodal weights (purple).

## 7 IMPLEMENTATION

Here, we give details about the discretization and form-finding algorithm that are part of our design system.

### 7.1 Discretization

Our discretization of plane elastic rods is similar to that of Bergou et al. [2008], and we distinguish between nodal quantities and edge quantities. This discretization is not needed for implementing the results from Sections 4 and 5, but we use it to discretize the stability criterion and its adjoint (Section 6), as well as for numerical testing with forward simulation.

A curve is represented as a polygonal chain (Fig. 12) with edge lengths $l_i$, which function as weights for edge quantities. Nodal quantities have as weights the Voronoi area $w_i$ of a node, i.e., half the sum of incident edge lengths. The bending energy and endpoint constraints of a rod are discretized as

$$W = \frac{1}{2}\sum_{i=0}^{n} K_i \frac{(\alpha_{i+1}-\alpha_i)^2}{w_i} \quad \text{and} \quad \sum_{i=1}^{n} l_i \begin{pmatrix}\cos\alpha_i \\ \sin\alpha_i\end{pmatrix} = \gamma_l,$$

where $K_0, \ldots, K_n$ are nodal stiffnesses; $\alpha_1, \ldots, \alpha_n$ are edge angles; and $\alpha_0$ and $\alpha_{n+1}$ are angle boundary values. The solution $\zeta$ to Eq. 7 is an edge quantity, with one fictitious edge added on either side of the curve. This gives samples $\zeta_0, \ldots, \zeta_{n+1}$, with $\zeta_0 = 0$ and $\zeta_1 = w_0$ by the initial conditions, and

$$-\frac{1}{l_i}\left(K_i \frac{\zeta_{i+1}-\zeta_i}{w_i} - K_{i-1}\frac{\zeta_i - \zeta_{i-1}}{w_{i-1}}\right) - \langle \lambda, \gamma_i' \rangle \zeta_i = 0,$$

with $\gamma_i' = (\cos\alpha_i, \sin\alpha_i)$, which can be solved for $\zeta_{i+1}$. The same edge discretization is used for $\eta_i$. Finally, $M_i$ and $N_{ij}$ are nodal quantities, which are computed by summing over edges in the same manner as for the endpoint constraints. The adjoint quantities can be discretized in the same way as the primal quantities. To compute $\delta F[\delta K]$, the derivatives $\alpha', \bar{\alpha}', \zeta', \bar{\zeta}'$, etc. are computed as nodal quantities, and initial values like $\zeta_0' = 1$ can be recovered exactly from the fictitious border edges that were added earlier.

### 7.2 Implementation of the Design System

The algorithms for computing a stiffness profile with or without gravity can be implemented by sampling an input curve and setting up the corresponding linear programs from Eqs. 4 and 6. We solve these programs to optimality using the Gurobi library.

Our design system offers different modes of user interaction. On the one hand, the user can directly edit a design by manipulating the control points of spline curves or surfaces, and modifying planes that are intersected with input surfaces to yield curves. The program generates a preview of the beam geometry necessary to realize these curves in a split second (see Fig. 16), which allows for a fast and interactive workflow.

The user can also give more control to the application by running a fabricability optimization routine that improves the design automatically. This is especially useful if the optimal stiffness ratio $R = \frac{\sup K}{\inf K}$ of a curve is too high for the chosen fabrication method, and the user cannot decrease it further with manual edits. At the core of this optimization method is a local/global approach.

**The local step** computes the derivative of $R$ with respect to coordinates of the spline control points, and modifies them using gradient descent with line search. The parameters $a$ and $b$ are modified as little as possible in the process. E.g., if there is a single inflection point, only $b$ is modified so $L$ still intersects the inflection point after the control points have been updated. These minimal changes to $a$ and $b$ are accounted for when computing the gradient.

**The global step** solves the linear program in Eq. 4 to regain the global optima for $a$ and $b$, while keeping the control points fixed. This step is only necessary if there are fewer than two inflection points, because otherwise $a$ and $b$ are defined up to positive multiples by the inflection line.

Neither step can increase $R$, given a small enough step size. For inflectional curves, we call EnforceConstraints after the local step. Optimization stops once a user-defined target stiffness ratio has been reached, or after a fixed number of iterations. We account for gravity in a post-process, by solving for $K$ once more with the linear program from Eq. 6 after the local/global algorithm terminates.

Naturally, the user can mix these modes of interaction freely, in order to converge to the best possible design. Once a design is finalized, the system outputs CAD files that include the outlines of all beams in their flat configuration, and the placement and orientation of fixtures for all beam endpoints.

## 8 FABRICATION & VALIDATION

Next, we present ways of manufacturing elastic strips that exhibit the stiffness profiles we have computed in previous sections. We show two methods that let us control the stiffness and width of a strip independently, by using either perforation or layering. To quantify the accuracy of deformed shapes, we 3d scanned physical models and compared them with the intended design. We also present numerical tests to assess the robustness of fabrication using elastic strips. Extensions that allow the use of nonlinearly elastic materials and account for mild plasticity effects are discussed in Appendix D.

### 8.1 Fabrication

The most straight-forward way of producing an elastic strip is to cut it from a sheet with constant thickness $h$, such that the width $w(s)$ of the strip is directly proportional to the stiffness $K(s)$. This achieves the desired behavior because $K \sim wh^3$ for elastic rods with a rectangular cross section.

The disadvantage of this method is that we relinquish direct control over the appearance of the strip, because all degrees of

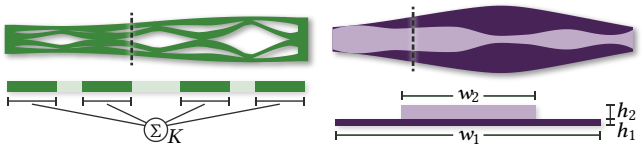


Fig. 13. **Perforated and Composite Strips.** *Top:* Examples of perforated *(left)* and composite *(right)* strip with section lines. *Bottom:* Cross sections.

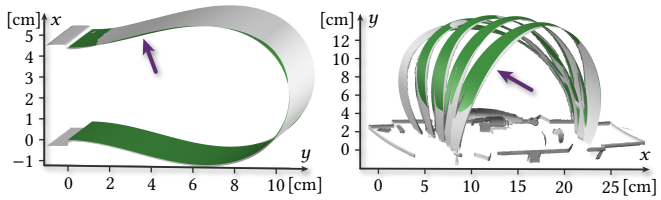


Fig. 14. **3d Scans.** Scans of physical models (gray) superimposed with simulated equilibrium shape (green). Arrows show maximal displacement error. *Left:* Cardboard model of arch with two inflections (max err. 1.7 mm). *Right:* Five interlocking arches of pavilion example (max err. 2.5 mm).

freedom go into realizing the stiffness. In particular, this makes it impossible to close gaps between adjacent strips in a model, because we cannot control the width independently of the stiffness. We found two ways to circumvent this limitation, shown in Fig. 13.

*Perforated Strips.* To prescribe the width and stiffness independently, we can remove material from a strip with width $w(s)$ by adding holes in order to achieve an *effective stiffness* $K(s)$. Our design removes diamond-shaped regions of material to reveal a network of smaller-scale strips, such that the total width integrated over a cross section is proportional to $K$, see Fig. 13 (left). We chose this type of perforation so the smaller-scale strips are approximately aligned with the direction of the main strip, in order to ensure uniform bending.

*Composite Strips.* Another way of decoupling $w$ and $K$ is to use a composite of two strips that are rigidly glued, see Fig. 13 (right). We use a broader strip (purple) with thickness $h_1$ and width $w_1(s)$ to determine the outer shape of the strip, and a narrower strip (lilac) with thickness $h_2$ and width $w_2(s)$ to add stiffness control. The stiffness of the composite strip can be approximated by[3]

$$cK = w_2(h_1 + h_2)^3 + (w_1 - w_2)h_1^3 = P_1 w_1 + P_2 w_2,$$

with $P_1 = h_1^3$, $P_2 = (h_1+h_2)^3 - h_1^3$, and $c$ a scaling constant. We want to prescribe $K$ and $w_1$, and compute $w_2$ subject to $0 \le w_2 \le w_1$ to satisfy this equation with some $c > 0$. The bounds on $w_2$ lead to constraints on $c$,

$$c_{\min}(s) := \frac{P_1 w_2(s)}{K(s)} \le c \le \frac{(P_1 + P_2)w_2(s)}{K(s)} =: c_{\max}(s),$$

for all $s \in [0, l]$. These constraints can be satisfied simultaneously if and only if $\max c_{\min} \le \min c_{\max}$. If this is the case, we use

[3]In this formula, we neglect the small offset between the overhang of the broad strip and the neutral line of the cross section. Instead, we assume that all mass is symmetrically distributed around the neutral line.

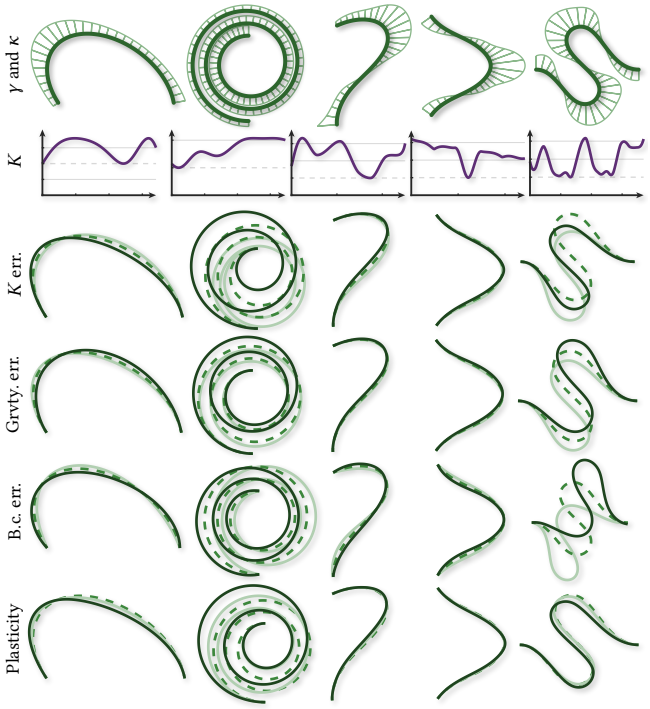


Fig. 15. **Robustness Study.** We show the effect of fabrication errors and parameter uncertainties on elastic curves on five representative examples. *Rows 3–6*: original curve (dashed) and curve affected by errors. *Top to bottom*: Curve and curvature normals; stiffness profile; stiffness range smaller (light green) or larger (dark green) than intended by 50%; gravity parameter underestimated (light) or overestimated (dark) by 50%; boundary angles off by 10°; plasticity affecting top 25% (light) or top 50% (dark) of curvature.

$c := \min c_{\max}$, which makes the narrow strip as wide as possible without protruding beyond the broad strip, as shown in Fig. 13 (right). Should the problem be infeasible, one can either change the design or reduce the thickness of the broad strip relative to that of the narrow strip. This works because the problem always becomes feasible as $h_1/h_2 \to 0$. All of our results that use composite strips were realized with $h_1/h_2 = 1/2$.[4]

## 8.2 Validation

*3d Scans.* To better quantify the predictive capabilities of our model, we used a dual-camera light scanner to capture the geometry of two physical models in their deformed state. The scanned models were then registered to the 3d models that served as input for computing the stiffness profiles. Fig. 14 shows a superimposition of the scanned and input models.

The first scan is of an arch with two inflections and a total length of 25 cm, yielding a maximum displacement error of 1.7 mm; this is about 1% of the model diagonal. The second scan shows a section of the pavilion example, composed of five interlocking elastic

[4]The gravity potential of a composite strip is linear in the unknown, $w_2$, so the model from Section 5 can easily be adapted to solve for $w_2$ of a composite strip with $w_1$ given.

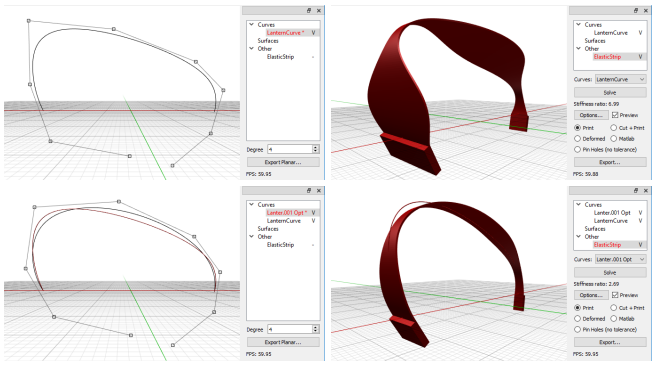

Fig. 16. **Lantern Design Session.** *Top:* B-Spline curve modeled by the user (left) and optimal stiffness profile computed by Eq. 4 (right). *Bottom:* Result of automatic fabricability optimization to guarantee $R \leq 3$.

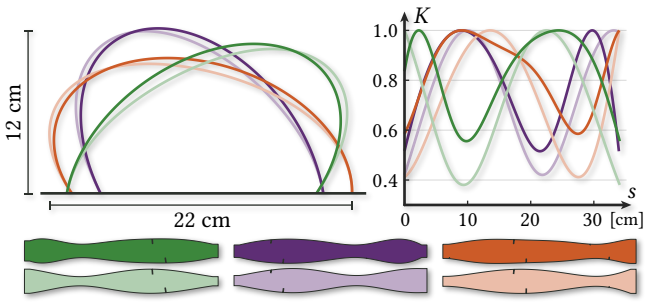


Fig. 17. **Pavilion.** *Top left:* Three arches from the pavilion model (dark); poor shape reproduction if gravity is neglected during optimization (light). *Top right:* Stiffness profiles computed with gravity (dark) and without gravity (light). *Bottom:* Final strip geometry with cuts for interlocking.

strips, each approximately 34 cm in length. Here, the maximum displacement error is 2.5 mm, also about 1% of the model diagonal.

*Numerical Testing.* In addition to conducting 3d scans, we performed a series of numerical tests that simulate the effects of material parameter uncertainty and fabrication error. This helps analyze the robustness of the fabrication process with elastic strips. Fig. 15 shows a few representative equilibrium curves, taken from the examples we show in Section 9. They include curves with zero to three inflection points, and one curve with a high turning number. In particular, we show the consequences of the following defects (rows 3–6):

- The ratio between minimal and maximal stiffness is lower (higher) than assumed.
- The gravity parameter $\frac{\rho}{Eh^2}$ is lower (higher) than assumed.
- The enforced boundary angles are defective.
- The highest-curvature regions deform plastically.

The exact impact of these errors will depend on the equilibrium curve in question, but we found curves with high total variation of turning angle, $\mathrm{V}(\alpha) = \int_0^l |\kappa|$, to be affected the most. On the other hand, inflection points close to the endpoints of a curve (e.g., column 4) seem to have a stabilizing effect.

## 9 RESULTS

We combine the design methods from Sections 4–7 and the fabrication techniques from Section 8 to manufacture physical models that demonstrate applications in architecture, model building, and interior design. Our stiffness construction algorithm reacts to user edits within a fraction of a second, which allows for fast iteration on the design of these models, and a quick evaluation of ideas. We also use the fabricability optimization routine of our design system (see Section 7.2) in order to suggest trade-offs between the original concept and ease of fabrication. For a detailed summary of all results, along with material, size, complexity, and computation times, consult Table 1.

We showcase a variety of materials such as cardboard, paper, polyacetal, and plywood, as well as different design processes such as approximation of existing 3d models, and direct specification using mathematical expressions. Some models use perforated or composite strips for maximal control, while others benefit from the naturally emergent shapes dictated by the stiffness distribution. Many of the models are between 50 and 100 cm in length, which would make it cost-prohibitive to 3d print all beams in their curved state, or to manufacture molds for all of them. Photographs of the physical models are shown in Figs. 1 (left) and 24, and renderings of two additional examples in Figs. 1 (right) and 23.

### 9.1 Emergent Strip Designs

We designed two objects that take their elastic strip geometry directly from the stiffness profiles computed with linear programming.

*Lantern.* The first is a lantern encased by twenty strips lasercut from a POM sheet with a thickness of 0.5 mm. The shape of the elastic strips was drafted in our software design tool using B-Spline curves, as seen in Fig. 16. The tool gives immediate visual feedback about the geometry of the strip resulting from the current design. The user can then either manually adapt the design to achieve better fabricability and appearance, or use the automatic optimization routine to decrease the max-to-min stiffness ratio of the strip. For this example, the optimization terminates under 1 second, giving real-time feedback and enabling an iterative design loop.

*Pavilion.* The second object is a pavilion composed of 31 interlocking cardboard strips that form an archway about one meter long, and 15 cm high. Every strip is designed as a segment of an ellipse, rotated around its center point, which gives the model a corkscrew-shaped appearance. The design uses 200 gsm cardboard, which is flexible enough for gravity to play a significant role, so we used the model from Section 5 to compute the width profile of every strip. Fig. 17 shows the effect of gravity, along with the resulting stiffness and width profiles.

The strips are spaced closely enough so neighboring strips intersect by a few millimeters each. These intersections are found computationally and show up as slotted cuts in the final model, to allow the strips to interlock. Note that little to no force is transmitted through these cuts, because every strip is in equilibrium even without neighboring strips as support. Fig. 14 validates the physical shape by 3d scanning.

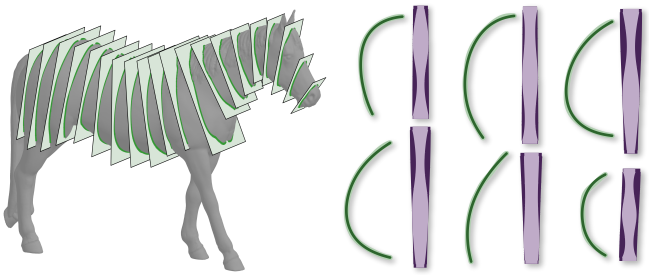

Fig. 18. **Horse.** *Left:* 3d model with planes and intersection curves. *Right:* A selection of input curves (light green) and optimized equilibrium curves satisfying $R \leq 2$ (dark green); composite strips realizing these curves (purple).

## 9.2 Composite Strip Designs

If the goal is to cover a closed 3d model with elastic strips, it is useful to have explicit control over the width profile of every strip, so gaps between strips can be minimized. We can achieve this by using composite strips, as discussed in Section 8, and demonstrate the technique on two 3d models.

*Horse.* This object is based on a pre-existing 3d model of a horse[5] that was not modified by the authors in any way prior to approximating it with equilibrium curves. To design the strip model, we specify a family of twenty planes spanning the body, neck, and head of the model, and compute the intersection curves, as shown in Fig 18. All remaining steps are automatic, except for choosing parameters such as spline curve degree and step sizes.

Each intersection curve is split at the spine, yielding a total of fourty sampled curves, which are then smoothed to remove high frequencies and approximated by quartic spline curves. Curves that do not have the equilibrium curve property initially are post-processed by removing spurious inflection points. Then, we run the auxiliary routine to optimize fabricability (see Section 7.2) until a value of $R \leq 2$ is reached for each curve. As Fig. 18 shows by example, most curves only change slightly as a result. The final step is to solve for $w_2$ of the composite strip as described in Section 8.1.

[5]https://free3d.com/3d-model/palomino-horse-walking-v1–643031.html

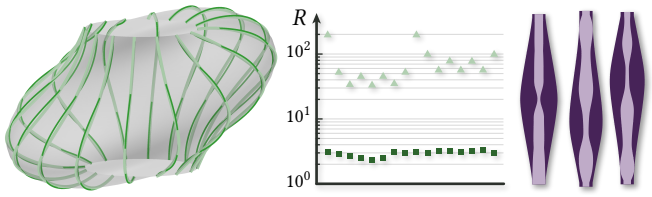


Fig. 19. **Flower Pot.** *Left:* NURBS model with input curves (light green) and optimized curves (dark green). *Center:* Stiffness ratio objective $R$ of all curves before optimization (light) and after optimization (dark). *Right:* Three composite strips used in the physical model.

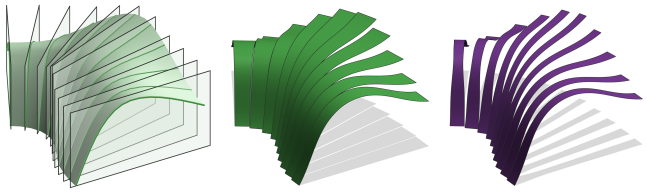

Fig. 20. **Shell.** *Left:* 3d model partitioned into ten sections. *Center:* Coverage of each elastic strip after fabricability optimization, using composite or perforated strips. *Right:* Sparse coverage if width is proportional to stiffness.

The physical model consists of 3d printed parts for the legs and tail of the horse, as well as a slender frame structure to hold the elastic strips. The composite strips are cut from 200 gsm cardboard and 100 gsm paper using a Cricut cutting machine, and then glued in their flat state. After insertion in the frame, they form the body, neck, and head of the horse. Some strips are tilted relative to the direction of gravity. This causes out-of-plane forces, but their effect is negligible on this scale, so planarity of deformations is retained.

*Flower Pot.* We designed this model by intersecting an asymmetric NURBS surface with radially arranged planes, which gives a total of 16 curves that we want to approximate as closely as possible with elastic strips (see Fig. 19). All curves initially satisfy the conditions

Table 1. **List of Results.** Summary of all models. Design: Curves based on 3d models, on analytical expression, or modeled directly by hand. #Strips: Total (Individually optimized). #SpC: Number of samples per curve. Size: length x width x height. Timings for stiffness computation, fabricability optimization, geometry processing, and sum of all three.

| Name | Material | Design | Grvty. | Fabrication | #Strips | #SpC | Size [cm] | Stfns. | Fbrcblty. | Gmtry. | Total |
|---|---|---|---|---|---|---|---|---|---|---|---|
| Shell | Cardboard | Model | No | Perforated | 60 (10) | 200 | 50x49x10 | 0.05 s | 1.39 s | 0.57 s | 2.01 s |
| Flower Pot | Cardboard | Model | Yes | Composite | 16 (16) | 500 | 30x27x17 | 1.26 s | 13.3 s | 1.46 s | 16.0 s |
| Horse | Cardboard | Model | No | Composite | 40 (40) | 200 | 56x14x39 | 0.15 s | 2.84 s | 11.6 s | 14.6 s |
| Pavilion | Cardboard | Analytical | Yes | Emergent | 31 (31) | 200 | 91x23x14 | 0.30 s | - | 3.93 s | 4.23 s |
| Lantern | POM | Direct | No | Emergent | 20 (2) | 240 | 28x28x26 | 0.003 s | 0.47 s | - | 0.47 s |
| Lamp | Plywood | Model | No | Perforated | 32 (32) | 200 | 93x66x17 | 0.11 s | 14.0 s | 0.12 s | 14.2 s |
| Vase | Cardboard | Analytical | No | Emergent | 20 (1) | 1.3k | 26x26x14 | - | - | - | 0.01 s |
| Carpet | - | Model | Yes | - | 15 (15) | 400 | 46x29x12 | 0.89 s | 2.47 s | 1.76 s | 5.12 s |
| Façade | - | Direct | No | - | 8 (8) | 300 | 55x12x43 | 0.17 s | 7.36 s | 1.33 s | 8.86 s |

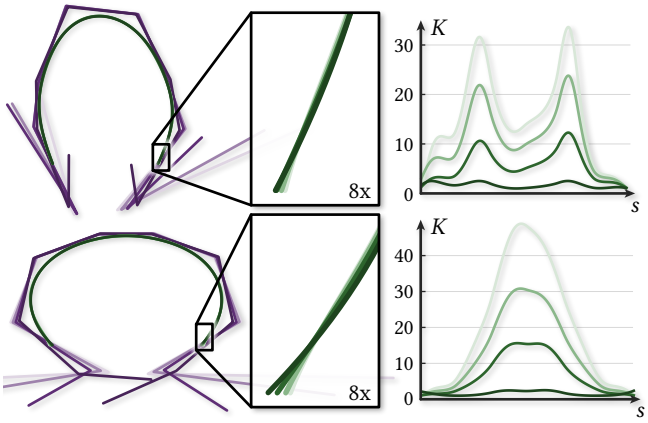


Fig. 21. **Lamp Optimization.** *Left:* Evolution of equilibrium curve (green) and its control polyline (purple) during fabricability optimization, from initial state (light) to final state (dark). *Right:* Evolution of stiffness profile $K$, normalized to $\min K = 1$.

of Theorem 1, but the optimal values of $R$ lie between 30 and 110, making it impractical for fabrication.

We opt to run automatic fabricability optimization to guarantee $R \leq 3.5$ for all 16 strips, which takes 13 s in total. The curves change slightly in the process, as shown in Fig. 19, but the overall shape of the object is preserved. Finally, we use the technique from Section 5.3 to arrive at a smooth stiffness profile, and compute the shapes of composite strips as discussed in Section 8.1.

## 9.3 Perforated Strip Designs

Another way of decoupling stiffness and strip width is to use perforation, which gives the physical object a more stylized appearance. We demonstrate this technique by manufacturing a miniature of an architectural shell from cardboard, and a large ceiling lamp made from plywood.

*Shell.* This model is based on a curved shell with three-fold mirror symmetry, initially given as a quad mesh. Fig. 20 (left) shows one sixth of the shell, along with a partition into ten slender sections. Each section grows wider towards the far end, which would cause large gaps between strips if the stiffness profile was used to directly determine strip width. To achieve better coverage (center), and an even distribution of material across the shell, we use the perforation technique described in Section 8.1.

The physical model shown in Fig. 24 (row 2) has a uniform texture with no large gaps and contains regions of both negative and positive apparent curvature. In total, sixty strips of 200 gsm cardboard with diamond-shaped cutouts are used to form the curved surface.

*Lamp.* Our largest model, with a footprint of 93 x 66 cm and a height of 17 cm, uses a 3d printed base with a thickness of 7 mm, and 32 elastic strips that have been lasercut from 0.8 mm plywood. Furthermore, the base is clad in a plywood veneer, so the lamp appears to be entirely done in woodwork. Without the use of active bending, a model like this would be extremely costly to make, requiring individual molds for all curved elements.

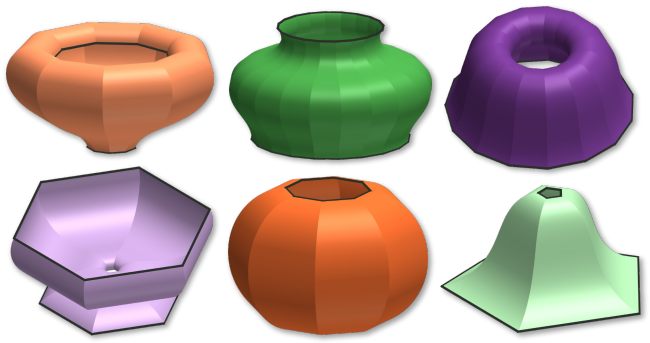

Fig. 22. **Surfaces of Revolution.** Examples of surfaces of revolution that can be tessellated without gaps. Lines mark kinematic boundary conditions.

The design takes an existing shell model [Gavriil et al. 2020], which was not modified by the present authors, and approximates planar sections with equilibrium curves. As shown in Fig. 21, the stiffness profiles of these curves can be significantly improved by tiny changes near the endpoints. Our optimization algorithm does this automatically, in less than 0.5 s per curve.

## 9.4 Surfaces of Revolution

Elastic strips with constant thickness can be used to tessellate a family of surfaces of revolution without gaps. We can characterize this family with a small modification to Eq. 3. Note that the tessellation constraint requires the width $w(s)$ of each strip to be directly proportional to the distance from the axis of revolution (cf. Fig. 22). If we identify the axis of revolution with $e_2$, and a direction orthogonal to it with $e_1$, this constraint reads $\langle e_1, \gamma(s)\rangle \sim w(s)$, where $w$ is proportional to $K$. Plugging this into Eq. 3 yields

$$\langle e_1, \gamma\rangle\kappa = a + \langle b, \gamma\rangle,$$

where the proportionality constants have been absorbed into the right-hand side. We can use this equation to generate all surfaces of revolution with the tessellation property by picking $a$, $b$, and initial conditions $\gamma(0)$ and $\alpha(0)$. Then, we integrate through the equation to solve for a meridian of the surface.

This application was inspired by Liu et al. [2020], who show a construction for surfaces of revolution with at most one inflection point. As the examples in Fig. 22 and our physical model in Fig. 24 show, our construction also supports more than one inflection, assuming kinematic boundary conditions. The subfamily with symmetric b.c. on one end is described by restricting $b$ to multiples of $e_2$.

## 9.5 Applications in Lighting Design

Figs. 1 (right) and 23 show two more applications of active bending in the form of renderings. The first is a flowing pavilion design ("Carpet") realized with 15 inflectional curves whose lowest points hover just above ground. The gap in-between allows indirect light to enter through the back and flood the space underneath the structure.

We further explore the role of active bending in lighting design with a kinetic façade inspired by the work of Knippers et al. [2012]. Elastic beams are placed vertically to form a façade that can be actuated by compression, in order to control the amount of indirect

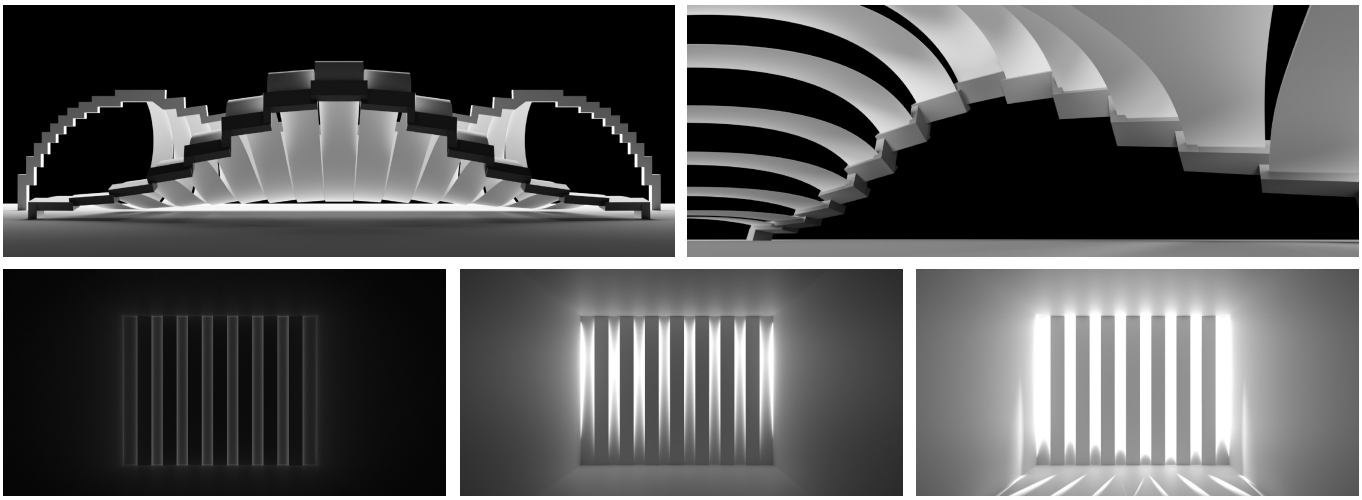

Fig. 23. **Renderings of Carpet and Façade.** *Top:* Carpet viewed from the front, and from the inside out. *Bottom:* Façade closed, partly open, and fully open.

light entering through. We used our design system to determine the deformed shape of the beams, to allow more light to enter through the top of the mechanism, as seen in Fig. 23 (bottom center).

## 10 DISCUSSION

In this work, we characterized the design space of plane elastic curves. Different spatial arrangements of these curves give rise to a variety of appealing forms, but we have yet to explore the possibilities offered by connecting elastic strips with joints, allowing them to undergo torsion, and accounting for the effect of creep over time. Understanding the complex design space offered by these mechanisms in geometric terms may offer new ways to support designers and enable flexible workflows with quick feedback loops. We believe that our approach to characterizing plane elastic curves geometrically can be generalized to the case of several jointed curves and non-planar deformations by considering appropriate variational problems and constraints.

Another useful extension would be to integrate standard beams, bending-active beams, and external forces in a single system. Possibly, our geometric characterization of bending-active beams can be combined with graphical statics to promote an intuitive understanding of these mixed constructions.

Furthermore, the present work does not consider the assembly process of bending-active structures. Deployment with light-weight mechanisms that respect stress bounds is an active area of research, and an essential part in the scaling up of designs with active bending.

In terms of application, we have only scratched the surface of kinetic structure design, in which actuation is used to alternate between different shapes. This idea offers an interesting challenge, because it is necessary to optimize structural elements for several deformed shapes at once, and to preserve the functionality of a design. A related problem is that of designing multi-stable elastic structures, which need only be actuated during a shape switch, but stay in each target shape without external force. We hope that our idea for stability optimization can contribute to this area of research.

## ACKNOWLEDGMENTS

We thank the anonymous reviewers for their generous feedback, and Michal Piovarči for his help in producing the supplemental video. This project has received funding from the European Research Council (ERC) under the European Union's Horizon 2020 research and innovation programme (grant agreement No 715767).

## REFERENCES

Marco Attene, Marco Livesu, Sylvain Lefebvre, Thomas Funkhouser, Szymon Rusinkiewicz, Stefano Ellero, Jonás Martínez, and Amit Haim Bermano. 2018. Design, Representations, and Processing for Additive Manufacturing. *Synthesis Lectures on Visual Computing* 10, 2 (2018), 1–146. https://doi.org/10.2200/s00847ed1v01y201804vcp031

B. Audoly and Y. Pomeau. 2010. *Elasticity and Geometry: From Hair Curls to the Nonlinear Response of Shells.* Oxford University Press. https://books.google.at/books?id=FMQRDAAAQBAJ

Milan Batista. 2015. On stability of elastic rod planar equilibrium configurations. *International Journal of Solids and Structures* 72 (2015), 144 – 152. https://doi.org/10.1016/j.ijsolstr.2015.07.024

Miklós Bergou, Max Wardetzky, Stephen Robinson, Basile Audoly, and Eitan Grinspun. 2008. Discrete elastic rods. In *ACM SIGGRAPH 2008 papers on - SIGGRAPH '08.* ACM Press. https://doi.org/10.1145/1399504.1360662

Amit H. Bermano, Thomas Funkhouser, and Szymon Rusinkiewicz. 2017. State of the Art in Methods and Representations for Fabrication-Aware Design. *Computer Graphics Forum* 36, 2 (2017), 509–535. https://doi.org/10.1111/cgf.13146

Florence Bertails, Basile Audoly, Marie-Paule Cani, Bernard Querleux, Frédéric Leroy, and Jean-Luc Lévêque. 2006. Super-helices for predicting the dynamics of natural hair. *ACM Transactions on Graphics* 25, 3 (2006), 1180–1187. https://doi.org/10.1145/1141911.1142012

Florence Bertails-Descoubes, Alexandre Jourdan, Victor Romero, and Arnaud Lazarus. 2018. Inverse design of an isotropic suspended Kirchhoff rod: theoretical and numerical results on the uniqueness of the natural shape. *Proceedings of the Royal Society A: Mathematical, Physical and Engineering Sciences* 474, 2212 (2018), 20170837. https://doi.org/10.1098/rspa.2017.0837

Gaurav Bharaj, David I. W. Levin, James Tompkin, Yun Fei, Hanspeter Pfister, Wojciech Matusik, and Changxi Zheng. 2015. Computational Design of Metallophone Contact Sounds. *ACM Trans. Graph.* 34, 6, Article 223 (2015), 13 pages. https://doi.org/10.1145/2816795.2818108

Bernd Bickel, Paolo Cignoni, Luigi Malomo, and Nico Pietroni. 2018. State of the Art on Stylized Fabrication. *Computer Graphics Forum* 37, 6 (2018), 325–342. https://doi.org/10.1111/cgf.13327

Max Born. 1906. *Untersuchungen über die Stabilität der elastische Linie in Ebene und Raum, unter verschiedenen Grenzbedingungen.* Göttingen, Dieterich'sche Univ.-Buchdruckerei.

Fig. 24. **Photographs of Physical Models.** *Top to bottom, left to right:* Pavilion, Horse, Shell, Vase, Lantern, Flower Pot, Lamp.

S.B. Coşkun. 2010. Analysis of Tilt-Buckling of Euler Columns with Varying Flexural Stiffness Using Homotopy Perturbation Method. *Mathematical Modelling and Analysis* 15, 3 (2010), 275–286. https://doi.org/10.3846/1392-6292.2010.15.275-286

Pierre Cuvilliers, Paul Mayencourt, and Caitlin Mueller. 2018. The Arc Lamp workshop at AAG 2018: active bending and digital fabrication. http://digitalstructures.mit.edu/page/blog#the-arc-lamp-workshop-at-aag-2018-active-bending-and-digital-fabrication Accessed: 2021-01-27.

Alexandre Derouet-Jourdan, Florence Bertails-Descoubes, and Joëlle Thollot. 2010. Stable Inverse Dynamic Curves. In *ACM SIGGRAPH Asia 2010 Papers* (Seoul, South Korea) *(SIGGRAPH ASIA '10)*. Association for Computing Machinery, New York, NY, USA, Article 137, 10 pages. https://doi.org/10.1145/1866158.1866159

Levi H Dudte, Etienne Vouga, Tomohiro Tachi, and Lakshminarayanan Mahadevan. 2016. Programming curvature using origami tessellations. *Nature materials* 15, 5 (2016), 583–588.

Moritz Fleischmann and Achim Menges. 2011. ICD/ITKE Research Pavilion: A Case Study of Multi-disciplinary Collaborative Computational Design. In *Computational Design Modelling*. Springer Berlin Heidelberg, 239–248. https://doi.org/10.1007/978-3-642-23435-4_27

Akash Garg, Andrew O. Sageman-Furnas, Bailin Deng, Yonghao Yue, Eitan Grinspun, Mark Pauly, and Max Wardetzky. 2014. Wire mesh design. *ACM Transactions on Graphics* 33, 4 (2014), 1–12. https://doi.org/10.1145/2601097.2601106

Konstantinos Gavriil, Ruslan Guseinov, Jesús Pérez, Davide Pellis, Paul Henderson, Florian Rist, Helmut Pottmann, and Bernd Bickel. 2020. Computational Design of Cold Bent Glass Façades. *ACM Transactions on Graphics (SIGGRAPH Asia 2020)* 39, 6, Article 208 (2020), 16 pages.

I. M. Gelfand and S. V. Fomin. 1963. *Calculus of Variations*. Prentice Hall.

Ruslan Guseinov, Connor McMahan, Jesús Pérez, Chiara Daraio, and Bernd Bickel. 2020. Programming temporal morphing of self-actuated shells. *Nature communications* 11, 1 (2020), 1–7.

Ruslan Guseinov, Eder Miguel, and Bernd Bickel. 2017. CurveUps. *ACM Transactions on Graphics* 36, 4 (2017), 1–12. https://doi.org/10.1145/3072959.3073709

Liang He, Huaishu Peng, Michelle Lin, Ravikanth Konjeti, François Guimbretière, and Jon E. Froehlich. 2019. Ondulé: Designing and Controlling 3D Printable Springs. In *Proceedings of the 32nd Annual ACM Symposium on User Interface Software and Technology*. ACM. https://doi.org/10.1145/3332165.3347951

Alexandra Ion, Michael Rabinovich, Philipp Herholz, and Olga Sorkine-Hornung. 2020. Shape approximation by developable wrapping. *ACM Transactions on Graphics* 39, 6 (2020), 1–12. https://doi.org/10.1145/3414685.3417835

David Jourdan, Melina Skouras, Etienne Vouga, and Adrien Bousseau. 2020. Printing-on-Fabric Meta-Material for Self-Shaping Architectural Models. In *Advances in Architectural Geometry*. http://www-sop.inria.fr/reves/Basilic/2020/JSVB20

Jan Knippers, Florian Scheible, Matthias Oppe, and Hauke Jungjohann. 2012. Bio-inspired Kinetic GFRP-façade for the Thematic Pavilion of the EXPO 2012 in Yeosu. In *Proceedings of the IASS-APCS-Symposium*, IASS (Ed.). Seoul, Korea.

Mina Konaković-Luković, Julian Panetta, Keenan Crane, and Mark Pauly. 2018. Rapid deployment of curved surfaces via programmable auxetics. *ACM Transactions on Graphics* 37, 4 (2018), 1–13. https://doi.org/10.1145/3197517.3201373

Joon Kyu Lee and Byoung Koo Lee. 2018. Elastica and buckling loads of nonlinear elastic tapered cantilever columns. *Engineering Solid Mechanics* 6 (2018), 39–50. https://doi.org/10.5267/j.esm.2017.11.001

Julian Lienhard, Holger Alpermann, Christoph Gengnagel, and Jan Knippers. 2013. Active Bending, a Review on Structures where Bending is Used as a Self-Formation Process. *International Journal of Space Structures* 28, 3-4 (2013), 187–196. https://doi.org/10.1260/0266-3511.28.3-4.187

Mingchao Liu, Lucie Domino, and Dominic Vella. 2020. Tapered elasticæ as a route for axisymmetric morphing structures. *Soft Matter* 16 (2020), 7739–7750. Issue 33. https://doi.org/10.1039/D0SM00714E

J. H. Maddocks. 1981. *Analysis of nonlinear differential equations governing the equilibria of an elastic rod and their stability*. Ph.D. Dissertation. University of Oxford.

Luigi Malomo, Jesús Pérez, Emmanuel Iarussi, Nico Pietroni, Eder Miguel, Paolo Cignoni, and Bernd Bickel. 2019. FlexMaps. *ACM Transactions on Graphics* 37, 6 (2019), 1–14. https://doi.org/10.1145/3272127.3275076

Robert S. Manning, Kathleen A. Rogers, and John H. Maddocks. 1998. Isoperimetric Conjugate Points with Application to the Stability of DNA Minicircles. *Proceedings: Mathematical, Physical and Engineering Sciences* 454, 1980 (1998), 3047–3074. http://www.jstor.org/stable/53424

Eder Miguel, Mathias Lepoutre, and Bernd Bickel. 2016. Computational design of stable planar-rod structures. *ACM Transactions on Graphics* 35, 4 (2016), 1–11. https://doi.org/10.1145/2897824.2925978

Dinesh K. Pai. 2002. STRANDS: Interactive Simulation of Thin Solids using Cosserat Models. *Computer Graphics Forum* 21, 3 (2002), 347–352. https://doi.org/10.1111/1467-8659.00594

J. Panetta, M. Konaković-Luković, F. Isvoranu, E. Bouleau, and M. Pauly. 2019. X-Shells: A New Class of Deployable Beam Structures. *ACM Transactions on Graphics* 38, 4 (2019), 1–15. https://doi.org/10.1145/3306346.3323040

Jesús Pérez, Miguel A. Otaduy, and Bernhard Thomaszewski. 2017. Computational design and automated fabrication of kirchhoff-plateau surfaces. *ACM Transactions on Graphics* 36, 4 (2017), 1–12. https://doi.org/10.1145/3072959.3073695

Jesús Pérez, Bernhard Thomaszewski, Stelian Coros, Bernd Bickel, José A. Canabal, Robert Sumner, and Miguel A. Otaduy. 2015. Design and fabrication of flexible rod meshes. *ACM Transactions on Graphics* 34, 4 (2015), 1–12. https://doi.org/10.1145/2766998

Stefan Pillwein, Kurt Leimer, Michael Birsak, and Przemyslaw Musialski. 2020. On elastic geodesic grids and their planar to spatial deployment. *ACM Transactions on Graphics* 39, 4 (2020). https://doi.org/10.1145/3386569.3392490

Yuri Sachkov and Stanislav Levyakov. 2010. Stability of inflectional elasticae centered at vertices or inflection points. *Proceedings of the Steklov Institute of Mathematics* 271 (2010), 177–192. https://doi.org/10.1134/S0081543810040140

Oded Stein, Eitan Grinspun, and Keenan Crane. 2018. Developability of triangle meshes. *ACM Transactions on Graphics* 37, 4 (2018), 1–14. https://doi.org/10.1145/3197517.3201303

Ioanna Symeonidou. 2015. Analogue and digital form-finding of bending rod structures. In *Proceedings of IASS Annual Symposia*, Vol. 2015. International Association for Shell and Spatial Structures (IASS), 1–12.

Nico Van der Aa, H.G. Morsche, and R.R.M. Mattheij. 2007. Computation of eigenvalue and eigenvector derivatives for a general complex-valued eigensystem. *The Electronic Journal of Linear Algebra* 16 (2007). https://doi.org/10.13001/1081-3810.1203

Guanyun Wang, Ye Tao, Ozguc Bertug Capunaman, Humphrey Yang, and Lining Yao. 2019. A-line: 4D Printing Morphing Linear Composite Structures. In *Proceedings of the 2019 CHI Conference on Human Factors in Computing Systems*. ACM. https://doi.org/10.1145/3290605.3300656

Katja Wolff, Roi Poranne, Oliver Glauser, and Olga Sorkine-Hornung. 2018. Packable Springs. *Computer Graphics Forum* 37, 2 (2018), 251–262. https://doi.org/10.1111/cgf.13358

Hongyi Xu, Espen Knoop, Stelian Coros, and Moritz Bächer. 2019. Bend-it: Design and Fabrication of Kinetic Wire Characters. *ACM Transactions on Graphics* 37, 6 (2019), 1–15. https://doi.org/10.1145/3272127.3275089

Xu Zheng, Zhichao Fan, Haoran Fu, Yuan Liu, Yanyang Zi, Yonggang Huang, and Yihui Zhang. 2019. Optimization-Based Approach for the Inverse Design of Ribbon-Shaped Three-Dimensional Structures Assembled Through Compressive Buckling. *Physical Review Applied* 11 (2019). https://doi.org/10.1103/PhysRevApplied.11.054053

## A PROOF OF GEOMETRIC CHARACTERIZATION

Here we give a proof of Theorem 1. It uses a short lemma, which we show first.

**Lemma 2.** *With the notation from Theorem 1, let $s_0 \in S_0$. Furthermore, let $(t, n)$ be the right-handed orthonormal basis adapted to $\gamma$ at $s_0$, i.e., $t = \gamma'(s_0)$. Then,* (1) *there exists a neighborhood of $s_0$, in which $s_0$ is the only root of $s \mapsto \langle \gamma''(s), n\rangle$;* (2) *it holds that*

$$\lim_{s\to s_0} \frac{\kappa(s)}{\langle \gamma''(s), n\rangle} = 1.$$

Proof. (1) We can find $\varepsilon > 0$ small enough, such that for all $s \in S_\varepsilon := (s_0-\varepsilon, s_0)\cup(s_0, s_0+\varepsilon)$, we have $\kappa(s) \neq 0$ and $\langle \gamma'(s), t\rangle > \frac{1}{2}$. Assume for the sake of contradiction that there exists $s_1 \in S_\varepsilon$ with $\langle \gamma''(s_1), n\rangle = 0$. Then, it follows from $0 \neq |\kappa(s_1)| = \|\gamma''(s_1)\|$ that $\langle \gamma''(s_1), t\rangle \neq 0$. This lets us compute

$$\langle \gamma'(s_1), t\rangle = \frac{1}{\langle \gamma''(s_1), t\rangle}\langle \gamma'(s_1), \gamma''(s_1)\rangle = 0,$$

because $\langle \gamma', \gamma''\rangle \equiv 0$. But this contradicts $\langle \gamma'(s_1), t\rangle > \frac{1}{2}$.

(2) By expressing $\kappa$ in the coordinate system $(t, n)$, we get

$$\frac{\kappa}{\langle \gamma'', n\rangle} = \frac{\det(\gamma', \gamma'')}{\langle \gamma'', n\rangle} = \langle \gamma', t\rangle - \frac{\langle \gamma', n\rangle\langle \gamma'', t\rangle}{\langle \gamma'', n\rangle}.$$

For the first term on the right-hand side, we have $\lim_{s\to s_0}\langle \gamma'(s), t\rangle = 1$. For the second term, write $\langle \gamma', \gamma''\rangle \equiv 0$ in coordinates to get

$$\langle \gamma', n\rangle\langle \gamma'', n\rangle + \langle \gamma', t\rangle\langle \gamma'', t\rangle = 0, \text{ so } \langle \gamma'', t\rangle = -\frac{\langle \gamma', n\rangle\langle \gamma'', n\rangle}{\langle \gamma', t\rangle},$$

where the denominator is non-zero in $S_\varepsilon$. Using this equality, the second term becomes

$$-\frac{\langle\gamma', n\rangle\langle\gamma'', t\rangle}{\langle\gamma'', n\rangle} = \frac{\langle\gamma', n\rangle^2}{\langle\gamma', t\rangle},$$

which goes to zero as $s \to s_0$, because $\langle\gamma'(s_0), n\rangle = 0$. This shows the statement. □

Proof of Theorem 1. **Direction "⇒":** Assume $\gamma$ is an equilibrium curve, so there exist $a \in \mathbb{R}$, $b \in \mathbb{R}^2$, and an admissible stiffness function $K$ with $K\kappa = a + \langle b, \gamma\rangle$. We show that then (1) and (2) hold. From $K > 0$, it follows that either $a \neq 0$ or $b \neq 0$, because otherwise $\kappa \equiv 0$, which contradicts that $S_0$ is finite.

**Case** $b = 0$: Then, $a \neq 0$, and $\kappa$ has the same sign as $a$ everywhere, so there are no zero-curvature points, and (2) is vacuously true. Choose any line $L$ that does not intersect $\gamma$ to satisfy (1).

**Case** $b \neq 0$**: Proof of (1):** The level sets of the function $f : \mathbb{R}^2 \to \mathbb{R} : x \mapsto a + \langle b, x\rangle$ form a family of parallel lines. Let $L$ be the zero-level set of $f$. We have $0 = K(s)\kappa(s)$ if and only if $s \in S_0$, and thus $0 = a + \langle b, \gamma(s)\rangle$ if and only if $s \in S_0$. This shows that $\gamma$ and $L$ intersect exactly in $\gamma(S_0)$.

Next, we show that $L$ is not tangent to $\gamma$ in any of the zero-curvature points. With the notation from Lemma 2, assume for the sake of contradiction that $L$ is tangent to $\gamma$ at $s_0$, i.e., $\langle b, t\rangle = 0$, which implies $b = \langle b, n\rangle n$.

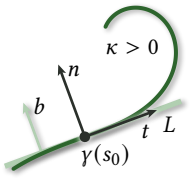


⌈**Claim:** $\langle b, n\rangle > 0$. **Proof of claim:** By $S_0$ finite, we know that $\kappa$ is non-zero in $(s_0, s_0 + \varepsilon)$ for $\varepsilon > 0$ small enough, so it does not change sign in this interval. If $\kappa > 0$ in $(s_0, s_0 + \varepsilon)$, then $\gamma$ winds counterclockwise in this interval, and thus $\langle\gamma - \gamma(s_0), n\rangle > 0$ in some interval $(s_0, s_0 + \varepsilon_1)$, because $(t, n)$ is right-handed. From $0 = a + \langle b, \gamma(s_0)\rangle$, it follows that

$$K\kappa = a + \langle b, \gamma\rangle = \langle b, \gamma - \gamma(s_0)\rangle = \langle b, n\rangle\langle\gamma - \gamma(s_0), n\rangle.$$

From $K\kappa > 0$, we see that $\langle b, n\rangle > 0$. The case $\kappa < 0$ in $(s_0, s_0 + \varepsilon)$ proceeds analogously: Then, $\gamma$ winds clockwise in $(s_0, s_0 + \varepsilon)$, so $\langle\gamma - \gamma(s_0), n\rangle < 0$ in some interval $(s_0, s_0 + \varepsilon_1)$. Because $K\kappa < 0$, we have $\langle b, n\rangle > 0$ again. This shows the claim. □⌋

Because $\langle b, n\rangle > 0$, and $K$ is bounded from below by a positive constant, there exists $A > 0$ such that for all $s \in (s_0, s_0 + \varepsilon_1)$,

$$\frac{\langle\gamma(s) - \gamma(s_0), n\rangle}{\kappa(s)} = \frac{K(s)}{\langle b, n\rangle} \geq A.$$

By Lemma 2, we know that

$$\liminf_{s\to s_0} \frac{\langle\gamma(s) - \gamma(s_0), n\rangle}{\langle\gamma''(s), n\rangle} = \liminf_{s\to s_0} \frac{\langle\gamma(s) - \gamma(s_0), n\rangle}{\kappa(s)} \geq A, \quad (8)$$

and that $\langle\gamma'', n\rangle$ does not change sign in some interval $(s_0, s_0 + \varepsilon]$. Let $s_\varepsilon$ be a maximizer of $|\langle\gamma'', n\rangle|$ in $(s_0, s_0 + \varepsilon]$. Note that a maximizer exists because $|\langle\gamma'', n\rangle|$ is continuous, and the supremum is not attained at $s_0$ because $\langle\gamma''(s_0), n\rangle = 0$. Then,

$$|\langle\gamma(s_\varepsilon) - \gamma(s_0), n\rangle| = \int_{s_0}^{s_\varepsilon}\int_{s_0}^{s_1} |\langle\gamma''(s_2), n\rangle| \,\mathrm{d}s_2 \,\mathrm{d}s_1 \leq \varepsilon^2 |\langle\gamma''(s_\varepsilon), n\rangle|,$$

where the equality follows from applying the fundamental theorem of calculus twice, and the inequality from bounding the integration area by $\varepsilon^2$, and the integrand by its maximum. This shows that $\frac{|\langle\gamma(s)-\gamma(s_0),n\rangle|}{|\langle\gamma''(s),n\rangle|}$ becomes arbitrarily small close to $s_0$, which implies

$$\liminf_{s\to s_0} \frac{\langle\gamma(s) - \gamma(s_0), n\rangle}{\langle\gamma''(s), n\rangle} = \liminf_{s\to s_0} \frac{|\langle\gamma(s) - \gamma(s_0), n\rangle|}{|\langle\gamma''(s), n\rangle|} = 0.$$

This contradicts Eq. 8, and our indirect assumption is proven false. We conclude that $L$ is not tangent to $\gamma$ in $s_0$.

**Proof of (2):** To show secant-boundedness of $\kappa$ at $s_0 \in S_0$, write[6]

$$\gamma'(s_0 + h) = \gamma'(s_0) + h\gamma''(s_0) + o(h) = t + o(h),$$

and, by integrating, $\gamma(s_0 + h) = \gamma(s_0) + ht + o(h^2)$. The equilibrium equation gives

$$K(s_0 + h)\kappa(s_0 + h) = a + \langle b, \gamma(s_0) + ht + o(h^2)\rangle = h\langle b, t\rangle + o(h^2).$$

Because of the non-tangency property, we have $\langle b, t\rangle \neq 0$, so the right-hand side is secant-bounded at $h = 0$. On the other hand, $K$ is bounded from below and above by positive constants. Thus, $\kappa$ is secant-bounded at $s_0$.

**Direction "⇐":** We assume that (1) and (2) hold and show the existence of $K$ admissible and $a \in \mathbb{R}$, $b \in \mathbb{R}^2$ that solve $K\kappa = a + \langle b, \gamma\rangle$. Because $\kappa$ is secant-bounded on $S_0$, it changes sign at every $s_0 \in S_0$. Because of the non-tangency condition, $\gamma$ crosses from one side of $L$ to the other at every $s_0 \in S_0$. Thus, the portion of the curve with $\kappa > 0$ lies fully on one side of $L$, and the portion with $\kappa < 0$ lies fully on the other. Choose $a$ and $b$ such that $L = \{x \in \mathbb{R}^2 : a + \langle b, x\rangle = 0\}$ and such that $a + \langle b, x\rangle > 0$ on the same side of $L$ as $\kappa > 0$.

Then, formally set $K(s) := \frac{a+\langle b,\gamma(s)\rangle}{\kappa(s)}$ for $s \in [0, l]$. Away from $S_0$, this function is positive and continuous, and thus bounded from above. Furthermore, $\kappa$ is continuous on $[0, l]$ and thus bounded, which implies that $K$ is also bounded from below by a positive constant, away from $S_0$.

It remains to show that $K$ is also bounded from above and below by positive constants as $s \to s_0 \in S_0$. By the same argument as above, we have

$$K(s_0 + h) = \frac{\langle b, t\rangle h + g(h)}{\kappa(s_0 + h)}, \quad \text{where} \quad g(h) = o(h^2). \quad (9)$$

Both numerator and denominator are secant-bounded at $h = 0$, and the signs of their secant bounds coincide. This is enough to guarantee that $K$ has the desired bounds. To see this, one analyzes $K$ as $h \to 0^+$ and $h \to 0^-$, for the cases where the secant bounds are either all positive or all negative.

For example, take the all-positive case and analyze $h \to 0^+$: There exist $d, D, e, E > 0$ and $\varepsilon > 0$ such that $dh < \langle b, t\rangle h + g(h) < Dh$ and $eh < \kappa(s_0 + h) < Eh$ for all $h \in (0, \varepsilon)$. Then, we can bound $d/E < K(s_0 + h) < D/e$. This shows that $K$ is admissible. □

## B ADJOINT EQUATIONS FOR CONJUGATE POINTS

We show how to compute $\partial\mathcal{Z}/\partial K|_{(\sigma,K)}$ by applying the adjoint method to the Euler–Lagrange equations and the Jacobi criterion. Let us define the functional $F[K] := \int \delta_\sigma(s)\mathcal{Z}(s, K)\,\mathrm{d}s$ with $\delta_\sigma$ the delta distribution centered at $\sigma$, so $\delta F/\delta K = \partial\mathcal{Z}/\partial K|_{(\sigma,K)}$. For easier

[6] We write $o(z(h))$ as a shorthand for some function $g(h)$ such that $\lim_{h\to 0} g(h)/z(h) = 0$. This means that $g(h)$ decays strictly faster than $z(h)$ as $h \to 0$. Therefore, if $f \in C^1$, then $f(x + h) = f(x) + hf'(x) + o(h)$.

implementation, $\delta_\sigma$ can also be replaced with a bump function that has small support, is centered at $\sigma$, and integrates to one.

The cofactors of the matrix $Z = \begin{pmatrix} \zeta & \eta_1 & \eta_2 \\ M_1 & N_{11} & N_{12} \\ M_2 & N_{21} & N_{22} \end{pmatrix}$ appear in the adjoint equations, and we will denote them by $C_{(\cdot)}$, e.g., $C_\zeta$ is the cofactor associated with the top-left entry $\zeta$ in $Z$. The adjoint variables will be denoted by overbars. First, we compute $\bar{M}_i$, $\bar{N}_{ij}$, $\bar{\zeta}$, and $\bar{\eta}_i$ via the following sequence of adjoint equations:

$$\begin{aligned} \bar{M}_i' &= \delta_\sigma C_{M_i}, & \bar{M}_i(l) &= 0, \\ \bar{N}_{ij}' &= \delta_\sigma C_{N_{ij}}, & \bar{N}_{ij}(l) &= 0, \\ -(K\bar{\zeta}')' - \langle \lambda, \gamma' \rangle \bar{\zeta} &= \textstyle\sum_k \bar{M}_k T_k - \delta_\sigma C_\zeta, & \bar{\zeta}(l) &= 0,\ \bar{\zeta}'(l) = 0, \\ -(K\bar{\eta}_i')' - \langle \lambda, \gamma' \rangle \bar{\eta}_i &= \textstyle\sum_k \bar{N}_{ki} T_k - \delta_\sigma C_{\eta_i}, & \bar{\eta}_i(l) &= 0,\ \bar{\eta}_i'(l) = 0. \end{aligned}$$

Then, we solve for the extremal of the variational problem

$$\begin{aligned} &\int_0^l \frac{1}{2}\left(K\bar{\alpha}'^2 - \langle \lambda, \gamma' \rangle \bar{\alpha}^2\right) \\ &\quad + \left[\bar{\zeta}\zeta \langle R\lambda, \gamma' \rangle + \textstyle\sum_i \bar{\eta}_i (\eta_i \langle R\lambda, \gamma' \rangle + g_i) \right. \\ &\qquad \left. + \textstyle\sum_i \bar{M}_i g_i \zeta + \sum_{ij} \bar{N}_{ij} g_i \eta_j \right] \bar{\alpha} \end{aligned}$$

$$\text{s.t.} \quad \begin{matrix} \bar{\alpha}(0) = 0, \\ \bar{\alpha}(l) = 0, \end{matrix} \quad \text{and} \quad \int_0^l T_i \bar{\alpha} = \int_0^l g_i \left(\bar{\zeta}\zeta + \textstyle\sum_k \bar{\eta}_k \eta_k\right) \text{ for } i = 1, 2$$

to compute $\bar{\alpha}$. Finally, the variational derivative of $F$ reads

$$\delta F[\delta K] = \left(\bar{\zeta}(0) + \textstyle\sum_i \bar{\eta}_i(0)\right)\delta K(0) + \int_0^l \left(\bar{\alpha}'\alpha' + \bar{\zeta}'\zeta' + \textstyle\sum_i \bar{\eta}_i'\eta_i'\right)\delta K.$$

## C CONSTRAINT SATISFACTION

Algorithm 2 calls the routine EnforceConstraints, which acts on the control points of a spline curve. Its objective is to restore the equilibrium property of the curve through collinearity of inflection points, and to enforce boundary conditions and fixed arc length.

We assume a spline parametrization $\gamma(t, q) = \sum_i B_i(t)\, q_i$ with $B_i$ piecewise polynomial and control points $q_1, \ldots, q_m \in \mathbb{R}^2$. For a total number of $N$ constraints, we denote the constraint manifold as $G(q) = 0$ with $G : \mathbb{R}^{2m} \to \mathbb{R}^N$, and its Jacobian as $J_G : \mathbb{R}^{2m} \to \mathbb{R}^{N \times 2m}$. Rows of $J_G$ corresponding to linear constraints may be precomputed at the beginning, and the remaining rows are updated every time the routine is called. First, we discuss all constraint types, and then the Newton-type iteration by which they are enforced.

*Collinearity of Inflections.* We over-constrain inflection points by keeping the inflection line $L$ constant during optimization. For each inflection, this produces one equality constraint of the form $G_{\text{infl}}(q) := a + \langle \gamma(t_0(q), q), b \rangle = 0$, where $t_0$ depends on $q$ implicitly via $\det(\gamma'(t_0, q), \gamma''(t_0, q)) = 0$. Derivatives can be evaluated as

$$\begin{aligned} \frac{\partial t_0}{\partial q_{i,j}} &= -\frac{1}{\det(\gamma', \gamma''')} \left[\det\left(\partial\gamma'/\partial q_{i,j}, \gamma''\right) + \det\left(\gamma', \partial\gamma''/\partial q_{i,j}\right)\right], \\ \frac{\partial G_{\text{infl}}}{\partial q_{i,j}} &= \left\langle \frac{\partial \gamma}{\partial q_{i,j}} + \gamma' \frac{\partial t_0}{\partial q_{i,j}}, b \right\rangle, \end{aligned}$$

where $q_{i,j}$ represents the $j$-th coordinate of $q_i$. Note that regularity of the constraint $G_{\text{infl}}(q) = 0$ is guaranteed by the upper bound on $R[K]$ that is introduced in Algorithm 2.

*Boundary Conditions.* Boundary points are fixed by constraints $\gamma(0) = \gamma_0$ and $\gamma(l) = \gamma_l$, and tangents by constraining $\langle \gamma'(0), n_0 \rangle = 0 = \langle \gamma'(l), n_l \rangle$, where $n_0$ and $n_l$ are the initial normals to the curve at its endpoints. These constraints are linear in $q$, so the derivatives $\partial\gamma/\partial q_{i,j}$ and $\partial\gamma'/\partial q_{i,j}$ can be precomputed at the beginning.

*Fixed Arc Length.* The arc length of a curve is discretized as $l(q) = \sum_{i=0}^{n-1} \|\gamma(t_{i+1}, q) - \gamma(t_i, q)\|$, and fixed with a constraint $G_{\text{arc}}(q) := l(q) - l_0 = 0$. Here $t_0, \ldots, t_n$ is a sampling of the parameter domain, and $l_0$ is the initial arc length.

*Enforcing Constraints.* The input to EnforceConstraints is a set of control points $q^0 \in \mathbb{R}^{2m}$ that might violate the constraints, and the goal is to find $q^n$ such that $G(q^n) = 0$, and $q^n$ close to $q^0$. We achieve this using an underdetermined Newton iteration $q^{i+1} = q^i + \Delta q$, where $\Delta q$ is the least-norm solution to $J_G\, \Delta q = -G$. This iteration does not converge to the orthogonal projection of $q^0$ onto $\{q \in \mathbb{R}^{2m} : G(q) = 0\}$, but it is a good approximation that can be computed robustly.

## D NONLINEAR MATERIALS

Our design system can be extended to account for certain material nonlinearities. We have not explored these models in our physical results, except for the spiral example shown in Fig. 7, which uses plasticity to account for the curvature of the innermost winding.

*Nonlinear Elasticity.* The left-hand side of Eq. 3 represents the internal moment $M(s) = K(s)\kappa(s)$ integrated over a cross section of an elastic strip. We can further decompose $K(s) = P\, w(s)$, where $w(s)$ is the width of the strip, and $P$ represents a linear material law.

A wide class of nonlinear material laws take the similar form

$$M(s) = P(\kappa(s))\, w(s)\, \kappa(s),$$

for $P : \mathbb{R} \to \mathbb{R}_{>0}$ an even function, and thus $P'(0) = 0$. This class includes for example strain-hardening behaviors ($P''(0) > 0$), and strain-softening behaviors ($P''(0) < 0$). Perhaps surprisingly, the theory developed in Section 4 applies to these laws as well, as long as the moment-per-unit-width function $m(\kappa) := P(\kappa)\kappa$ is injective in the relevant curvature range. If this is the case, we can solve for $a \in \mathbb{R}$ and $b \in \mathbb{R}^2$ using the same linear program, and then compute $w(s)$ from the equation $w(s)\, m(\kappa(s)) = a + \langle b, \gamma(s) \rangle$.

*Plasticity.* If an elastic strip is bent beyond the elastic limit of the base material, some of the deformation will become permanent, and the strip does not return to its original flat state after removing external forces. This effect was noticeable in our experiments with bending cardboard (200 gsm) for curvature radii below 2 cm.

The simplest plasticity model is that of an *ideally plastic* material, which assumes that the linear stress-strain law is replaced by a constant law at the elastic limit. Applied to elastic strips, this model postulates the existence of a curvature limit $\kappa_{\text{lim}}$, such that all curvature beyond this point becomes plastic. We implemented this model in our design system by replacing $\kappa(s_i)$ in Eq. 4 by an *effective curvature* $\kappa_{\text{eff}}(s_i) := \min\{\kappa(s_i), \kappa_{\text{lim}}\}$. This implementation does not account for path-dependent deformation during the bending process, or the formation of plastic hinges. As such, it is only an approximation of ideally plastic behavior.